# MASTER THESIS

---

# LINKING CHANGES IN MINERAL CHEMISTRY TO REACTIVITY: A STUDY ON CARBONATE INCORPORATION IN SYNTHETIC HYDROXYAPATITE AND ITS EFFECT ON SOLUBILITY


Jessica Klop
Utrecht University
Faculty of Geosciences
MSc Earth Structure & Dynamics

1st Supervisor: Dr. Helen King
2nd Supervisor: Dr. Peter Kraal

March 17, 2018

# I. ABSTRACT

The human skeleton is an important contributor to homeostasis in our bodies, as chemical elements can either be stored in the bone material or extracted when needed anywhere else. More than two-thirds of human bone mass consists of a mineral called hydroxyapatite. Ions such as carbonate can be incorporated into the apatite crystal structure by replacing other ions. Such substitution processes occur in every healthy body, but they can have significant effects on the bone mineral reactivity when excessive amounts of carbonate are incorporated, as is the case in patients with X-linked hypophosphatemia. The aim of this study was to find out how the incorporation of carbonate affects the solubility of hydroxyapatite minerals. Five samples were synthesised at 37 °C by a double decomposition reaction between a calcium chloride solution and a carbonate phosphate solution, which had a carbonate concentration ranging between 0 and 0.48 M. The precipitated minerals were imaged using atomic force microscopy and a Leica microscope and analyzed by Fourier transform infrared spectroscopy and Raman spectroscopy. Next, the samples were (partly) dissolved in a buffered sodium chloride solution with pH 6.5, while samples were collected at regular time intervals. Colourimetric determination of the phosphate concentration of these extracted sample solutions was done using the molybdenum blue method. Results from this study indicate the precipitation of octacalcium phosphate in the sample without added carbonate, instead of the expected apatite. This can be explained by the solution pH of 5.2 during sample synthesis and the fact that octacalcium phosphate is stable between pH 4 and 6.5, while hydroxyapatite only forms at pH values above 7.4. Furthermore, the spectroscopic data indicated that there was a positive correlation between the carbonate concentration during synthesis and the amount of incorporated carbonate for samples CO1 to CO3. Sample CO4 had the highest initial carbonate concentration, but this did not result in the highest carbonate content. Instead, sample CO2 and CO4 had similar amounts of incorporated $CO_3^{2-}$, despite their different initial carbonate concentrations. This observation was attributed to a pH increase of the synthesis solution in response to the increasing amount of carbonate in solution. It is suggested that the carbonate content is related to synthesis pH and that a maximum amount of $CO_3^{2-}$ incorporation occurs around pH 10-10.5. This can be attributed to the speciation of carbonate, as $CO_3^{2-}$ becomes more abundant than $HCO_3^-$ around a pH of 10.33, which could have inhibited the carbonate incorporation. Furthermore, the sample crystallinity decreases with increasing carbonate content. This is related to the increasing amount of structural defects that occurs in the apatite lattice as more carbonate is taken up in the structure. Carbonate often replaces hydroxide (A-type substitution) or phosphate (B-type substitution), but can also be incorporated in the external, less crystalline apatite layers (labile substitution). The spectroscopic data shows that B-type substitution is dominant in all samples, but relatively more A-type and labile carbonate is found in samples that were synthesised at higher pH. This subsequently resulted in a lower crystallinity for these samples. When exposed to the buffered solution with pH 6.5, a significant amount of phosphate was released during the first 10-20 minutes of the experiment. The sample without carbonate showed the highest dissolution rate during this phase, which is attributed to the high surface area of the platy minerals and the instability of octacalcium phosphate at pH values above 6.4. For the carbonated samples, CO3 experienced significantly higher dissolution rates than CO2 and CO4, while they had a similar crystallinity index. This can be attributed to the positive correlation between dissolution rate and carbonate content. Although crystallinity is likely to affect the dissolution process as well, it seems that the carbonate content is dominant in determining the mineral solubility. Therefore, this study concludes that bone minerals with a relatively high carbonate content will experience a significant increase in solubility. This is likely to speed-up the bone remodelling process, as the dissolution of the hydroxyapatite minerals occurs faster. For patients with X-linked hypophosphatemia, this will only contribute to the problem, as more carbonate will be incorporated to make up for the loss of phosphate during the faster bone remodelling process, which will subsequently increase the bone mineral solubility.

# II. ACKNOWLEDGEMENTS

This MSc thesis was written at the University of Utrecht, under the supervision of Dr. Helen King and Dr. Peter Kraal. The experiments were performed in the Gemeenschappelijk Milieulaboratorium and financial support was provided by the University of Utrecht, without who this research would not have been possible.

I have learned a lot throughout the duration of this research and I am grateful for all the help I received along the way. I would especially like to thank Helen King for her guidance. She provided me with the knowledge and confidence to work independently with big, expensive instruments and helped me see when the right track wasn't necessarily the original one. I would also like to give a big thanks to Peter Kraal, for his useful comments and never-ending enthusiasm.

Lastly, I want to express my gratitude towards my dear friends and family, who have supported me throughout my years of study. Thank you all for your support.

# III. TABLE OF CONTENTS

# IV. INTRODUCTION

## IV.I Research objectives

The human skeleton not only has a structural function by providing support to the body and protection of vital organs, it also serves a metabolic function by storing chemical elements such as calcium and phosphate (Hadjidakis, 2006). Keeping the concentration of ions in the bloodstream within a particular range is a process called homeostasis, where the balance is maintained by either incorporating ions in the bone minerals, or by withdrawing them for further use. The exchange of chemical elements between bone minerals and the blood serum happens when the old minerals are dissolved and new tissue is formed. This natural, continuous process is called bone remodelling and allows for the maintenance of the quality and size of the skeleton, for example by repairing microfractures (Hadjidakis, 2006). However, an imbalance in remodelling rates can result in weaker bone structures when the amount of material that is broken down exceeds the rate of formation, as is the case with osteoporosis. Osteoporosis is a disease in which bones progressively become more porous, greatly increasing the risk of fracture (International Osteoporosis Foundation (IOF) 1, 2017). According to the IOF, one in three women and one in five men are at risk of an osteoporotic fracture.

Another problem related to bone remodelling occurs when the newly formed bone minerals are chemically different from the old. This can considerably affect bone rigidity and strength, as is observed in patients with X-linked hypophosphatemia (XLH). This genetic disease is associated with a phosphate deficiency in the bloodstream, as the patient's body cannot contain the phosphate ions that are released during the bone remodelling process. The hardness and rigidity of bones is mostly provided by the presence of calcium and phosphate (International Osteoporosis Foundation 2, 2017). Therefore, a lack of phosphate and the subsequent uptake of other ions into the bone material can result in a weaker bone structure. Phosphate is often replaced by carbonate, which is substantially smaller and thus very likely to change the chemical properties of the newly formed bone material.

While research has been conducted on bone remodelling mechanisms previously, these studies did not focus on mineralogical changes and their effect on solubility in particular. Furthermore, most studies were done before the development of new analytical instruments, while these improved experimental techniques are expected to provide further insight into the processes that control dissolution. For example, solubility is often measured by the release of ions and by comparing the morphology of the particles prior to dissolution, to minerals that had been dissolving for several hours. Monitoring these morphological changes would be more precise with the use of AFM, which allows for continuous, *in situ* imaging of the dissolving particles.

The main aim of this research is to find out how changes in bone mineral chemistry affect the solubility of the material. More specifically, due to diseases such as X-linked hypophosphatemia, carbonate ions are incorporated into the bone mineral by replacing other molecules. Our aim is to find out how the incorporation of different amounts of carbonate affects the crystallinity and morphology of synthetic bone minerals and subsequently link these changes to differences in solubility. This will provide new insights into the effect of XLH on bone mineralogy and hopefully aid in the research of other bone-related diseases.

## IV.II Background information

In order to see how bone mineral chemistry is affected by certain diseases, it is important to understand how bones are formed in the first place. The structural components that make up our bones consist of collagen, cells and the extracellular matrix, which is largely mineralized. These mineralized parts are made of hydroxyapatite crystals ($Ca_{10}(PO_4)_6(OH)_2$) that are found within the matrix and on and within the collagen fibres, where they are often orientated in the same direction as the fibres (Hadjidakis, 2006). In general, bones have a strong, dense outer layer called the cortical (compact) bone, which surrounds the less dense inner layer called the trabecular (cancellous) bone (Adler, 2000). Even though these two types of bone have the same chemical composition, they have very different morphology and strength. Another difference is that trabecular bone has a high turnover rate and therefore has a major metabolic function. Cortical bone can also participate in metabolic processes, but does so at a slower pace and often only responds during times of severe or prolonged mineral deficit (Hadjidakis, 2006).

The cells that are responsible for bone matrix synthesis and mineralization are called osteoblasts. About 15% of mature osteoblasts are entrapped within the new layer of bone matrix that they produce, after which they differentiate into osteocytes (Hadjidakis, 2006). The produced bone matrix is called osteoid. It consists of collagen and non-collagenous proteins. Together with the osteocytes, the matrix material eventually mineralizes and calcifies into bone. The osteocytes form an extensive network and are connected to cells on the bone surface, allowing them to react to physical forces on the bone by initiating either resorption or formation processes (Raggatt & Partridge, 2010).

Osteoclasts are large multinucleated cells that are responsible for the resorption of the mineralized bone tissue (Väänänen, 2000). They are attached to the calcified bone surface through the sealing zone (Figure 1) that separates the extracellular fluid from the bone-resorbing compartment between the osteoclast and the bone material, which is called the resorption lacuna. Before being able to reach and dissolve the hydroxyapatite crystals, the osteoclast releases enzymes that break down the collagenous bone matrix (Baron, 1995). Then, hydrogen chloride (HCl) is secreted into the resorption lacuna through the ruffled border, which is named after its characteristic foldings (Figure 1a).

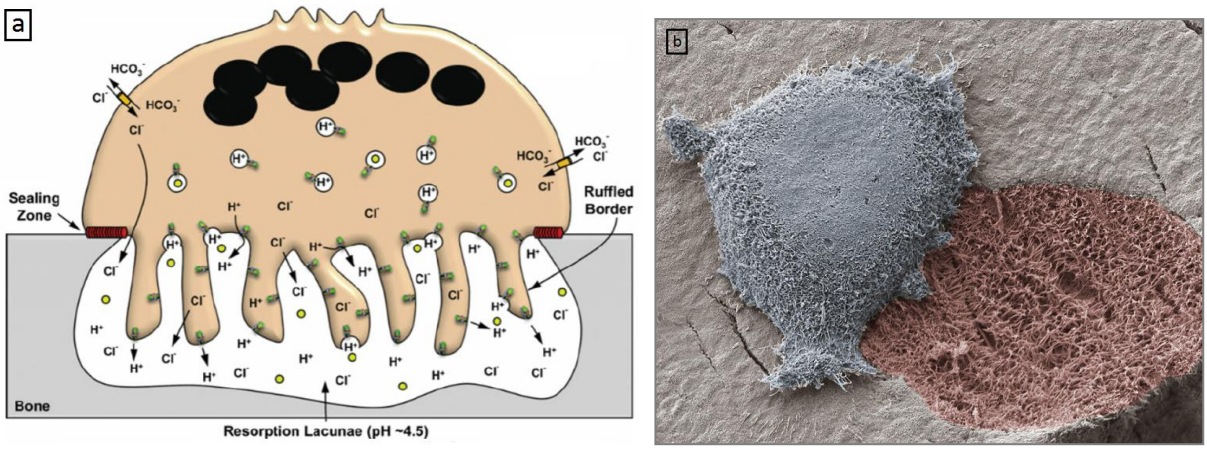


**Figure 1a (left): Schematic drawing of an osteoclast. The resorption lacuna is an extracellular space between the ruffled border membrane and the bone matrix. It is sealed from the extracellular fluid by the sealing zone. Adapted from Qin, 2012. Figure 1b (right): Scanning electron micrograph of an activated osteoclast (blue) on the bone mineral surface (white). The pink part is a resorption pit, where bone minerals have been resorbed by the moving osteoclast. Source: Bone Research Society, 2017.**

Although experiments have demonstrated the acidity of the resorption lacuna (Anderson, 1986; Baron, 1985) and it is generally accepted that a low pH promotes the dissolution of bone mineral, information on the exact chemical composition of the dissolution fluid is scarce, as it is difficult to examine these conditions *in situ*. Reportedly, the pH inside the resorption lacuna is roughly 4.5 (Qin, 2012). Väänänen (1990) describes the importance of proton pumps on the ruffled border in regulating the acidity of the resorption lacuna, as it pumps $H^+$ across the membrane. A neutral charge is maintained by chloride channels that provide $Cl^-$ (Baron, 1995). Also, *in vitro* research of isolated osteoclasts confirms that the resorption of bone only happens very locally within the sealing zone and without the contribution of other cells (Chambers, 1984). The amount of bone that is resorbed by an osteoclast depends on the bone type and its specific strength. In cortical bone, the osteoclasts gradually burrow through the bone with a speed of 20–40 µm/day, while in trabecular bone the resorption speed is slightly lower, with values of approximately 25 µm/day (Hadjidakis, 2006).

About 1 in 20,000 people are estimated to suffer from XLH (Carpenter, 1997). Often, the disease becomes noticeable in children over 18 months old, as they begin to show skeletal abnormalities such as bent legs, a short stature, and irregular growth of the skull. Instead of resolving with growth, the symptoms often get worse over time and can progress to include pain in the bones, joints, and teeth (Sharkey, 2015). In some cases (5-29%) patients suffer from recurrent bone fractures and hearing impairments (Köhler, 2017). Microscopic investigation of both trabecular and cortical bone specimen of patients with XLH characteristically show an increase in unmineralized bone matrix or osteoid, even though the total bone volume may be normal (Marie, 1981). This compromised bone mineralization has been attributed to a defect in the kidneys that prevents the absorption of filtered phosphate. This results in its excessive urinary excretion and eventually lowers the phosphate concentration in the blood serum (Carpenter, 1997). Subsequently, less phosphate is available in the bloodstream to be incorporated into the resorbing bone minerals, which increases the uptake of other ions such as carbonate.

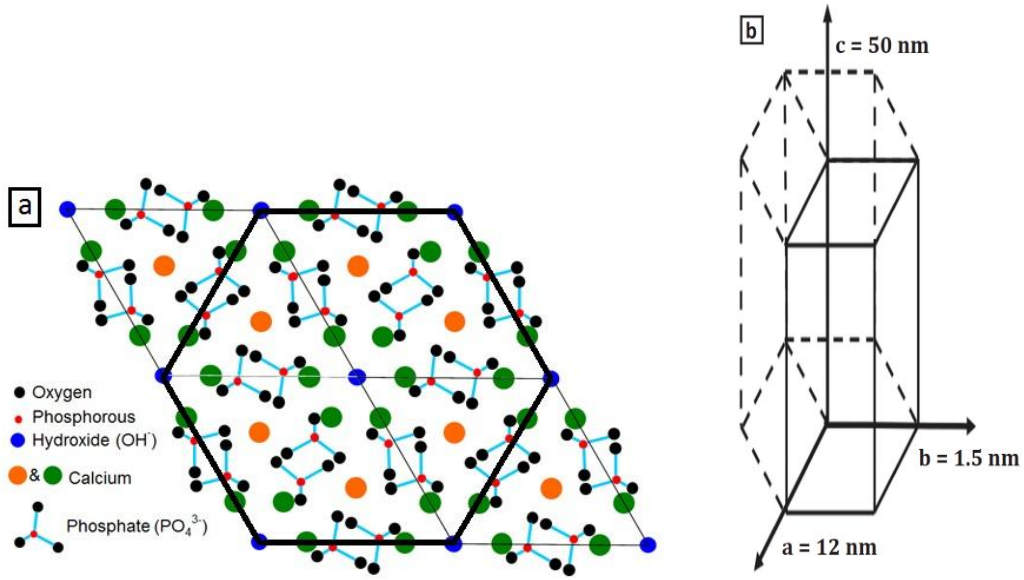


**Figure 2a (left): The hexagonal crystal lattice is typical for biological hydroxyapatite. Adapted from Wallace (2017). Figure 2b (right): An indication of the thickness and length of the a- and c-axes after mineral maturation of biological hydroxyapatite is displayed here.**

The type of hydroxyapatite that occurs in bone material is a non-stoichiometric form of apatite, which is often called biological apatite or poorly crystalline apatite (PCA) due to its calcium-deficiency (Cazalbou, 2004; Wallace, 2017). The molecules are arranged in a hexagonal crystal lattice (Figure 2a) during initial mineral formation. Over time, the c-axis of the crystals grows in comparison to the a-axis (Figure 2b) and the mineral matures into plate-like crystal shapes with a c-axis of roughly 50 nm. The length of the a-axis is then 12 nm, while the b-axis will only reach 1.5 nm (Wallace, 2017).

Biological hydroxyapatite (HA or HAp) can have a range of chemical properties, depending on the type of substitution that occurs at specific ionic sites. When carbonate substitutes for another ion such as phosphate or hydroxide, a carbonated type of hydroxyapatite is formed (CHAp). Biological apatite in natural bone often contains around 7.5 wt% carbonate (Sader, 2013; Yusufoglu, 2008). The carbonate ions are often incorporated via B-type substitution, where they replace phosphate (Elliot, 1994; Leventouri, 2006). The exact configuration of this substitution is a topic that has been debated extensively because of the different configuration and charge of the two ions. Phosphate is trivalent ($PO_4^{3-}$) and consists of one phosphorus atom and four oxygen atoms that are arranged in a tetrahedral shape, while carbonate ions are divalent ($CO_3^{2-}$) and are made up of one carbon atom surrounded by three oxygen atoms. Carbonate molecules have a trigonal, planar arrangement, as can be seen in Figure 3 (Skinner, 1989). Several locations have been proposed for the incorporation of $CO_3^{2-}$ in B-type carbonate, including the sloping and adjacent faces of the phosphate tetrahedron (Ivanova, 2001; Fleet, 2004). Leventouri (2006) contradicts these theories by proposing the $PO_4^{3-}$ mirror plane as possible substitution location.

A-type substitution is another form of carbonate incorporation, which means that that one $CO_3^{2-}$ molecule replaces two $OH^-$ ions (Elliott, 1964). Hydroxide consists of an oxygen and a hydrogen atom and is, therefore, smaller than carbonate (Figure 3). The differences in size and charge between carbonate, phosphate, and hydroxide are often resolved by creating vacant cation sites or by coupled substitution, where lower valence cations are incorporated into the structure along with carbonate to make up for the charge difference (Chickerur, 1980). These structural and chemical changes have a destabilising effect on hydroxyapatite minerals and significantly decrease their crystallinity. The effects of carbonate substitution are therefore reported by several studies as the main reason that carbonated apatite is more soluble than hydroxyapatite, especially in acidic solutions (Baig, 1996; Barry, 2002). Finally, several studies report a third and slightly different way in which carbonate can be present in hydroxyapatite minerals. Instead of occupying a stable place in the mineral lattice, this labile type of carbonate is thought to reside in less crystalline, external apatite layers (Rey, 1989).

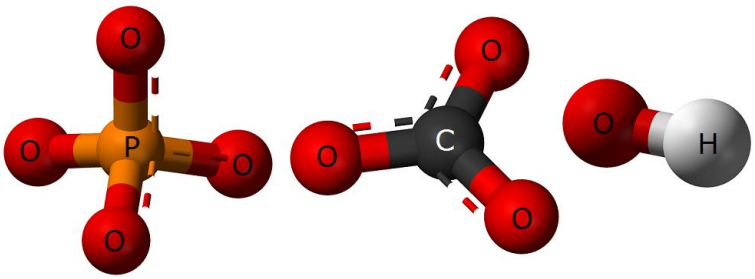


**Figure 3. Three-dimensional representations of phosphate, carbonate and hydroxide molecules, respectively. The letters indicate the type of atom, where P = phosphor, C =carbonate, H = hydrogen, O = oxygen. Source: National Center for Biotechnology Information, 2017.**

# V. METHODOLOGY

## V.I Sample synthesis

The hydroxyapatite samples were synthesised by double decomposition between a calcium solution and a carbonate-phosphate solution, following an adapted version of the method used by De Groot (2017). The calcium solution had a concentration of 0.1 M and was prepared by dissolving 1.3873 g calcium chloride ($CaCl_2$, provided by Merck) in 125 mL of UHQ (ultra-high quality $H_2O$). Using a pipette, this solution was divided over five separate septum bottles, which were closed off with a rubber stopper and metal cap. To reduce the amount of atmospheric carbon dioxide in the bottles, argon gas was pumped into the bottles through a needle for eight minutes, while the air was allowed to escape through a different needle. Next, five beakers were set aside and to each one, a distinct amount of sodium carbonate ($Na_2CO_3$, provided by Merck) was added (see Table 1). Then, 25 mL of a 0.12 M phosphate solution was added to each beaker, to obtain five different carbonate-phosphate solutions with carbonate concentrations of 0, 0.12, 0.24, 0.36 and 0.48 M. The phosphate solution was prepared by dissolving 2.1294 g disodium hydrogen phosphate ($Na_2HPO_4$, provided by Sigma-Aldrich) in 125 mL of UHQ. Finally, a reservoir was filled with water and placed on the IKA RT15 magnetic hotplate and stirrer. The water was heated to 37°C and the stirring plate was set to 300 rotations per minute (RPM), before placing the calcium solutions in the warm-water bath. Using a needle and syringe, 25 mL of each carbonate-phosphate solution was added to a separate septum bottle containing the calcium solution. These final solutions were left in the water bath at a constant temperature, while being stirred, until sampling.

| **Sample name** | **CO0** | **CO1** | **CO2** | **CO3** | **CO4** |
|---|---|---|---|---|---|
| Amount of $Na_2CO_3$ | 0 g | 0.3180 g | 0.6359 g | 0.9539 g | 1.2719 g |
| Carbonate concentration | 0 M | 0.12 M | 0.24 M | 0.36 M | 0.48 M |

**Table 1. Amount of $Na_2CO_3$ added to each sample to obtain the required carbonate concentration.**

The synthesis method by De Groot (2017) required multiple samples to be taken at regular intervals after mixing of the final solution. For this project, we were not interested in the changes of the precipitated minerals over time, but in the different characteristics of the final samples. Also, the synthesised samples would preferably only differ in carbonate content due to the amount of $Na_2CO_3$ that was added to the phosphate solution, and not due to different precipitation times. According to results by De Groot (2017), the carbonate content in the different samples should be almost constant after a time period of ~100 hours. Therefore, instead of sampling at regular intervals, the entire solution was sampled 4 days (96 hours) after mixing of the final solution.

The sampling was done using a needle and syringe. First, 10 mL of each solution was transferred to a centrifuge tube, resulting in five tubes that were intended for analysis by atomic force microscopy (AFM). The remaining 15 mL of each sample was transferred to another tube that was intended for the chemical analysis. Next, the centrifuge tubes were centrifuged for ten minutes at 3200 RPM and a temperature of 20°C, using a Thermo Scientific SL 40R centrifuge. The supernatant was not needed in this study and could be disposed of. The precipitates were rinsed with UHQ and a thin layer of UHQ was added to the tubes that were intended for AFM analysis, as this method required the particles to be in a slightly diluted suspension. Finally, all centrifuge tubes were stored in the freezer to prevent any further phase transformations. To find out if the pH of the solutions changed during sample synthesis, the synthesis process and first hour of precipitation were repeated. The calcium and carbonate phosphate solutions were prepared as before and their initial pH values were measured using a Consort C830 pH meter. Then, the solutions were mixed and their pH was checked at regular intervals for the duration of 60 minutes.

## V.II Chemical analysis

### *V.II.a FTIR spectroscopy*

A Nicolet 6700 Fourier transform infrared (FTIR) spectrometer was used to obtain one integrated, vibrational spectrum for each sample. The instrument was purged with nitrogen for 30 minutes before analysis, to reduce the amount of moisture and carbon dioxide in the sample chamber and minimize the level of background noise during analysis. Prior to each spectrum collection, the instrument was again purged for one minute. The amount of background noise was measured by placing a sample cup filled with potassium bromide (KBr, Spectra-Tech, 99%) in the instrument. The samples intended for the chemical analysis were taken from the freezer and defrosted. Then, a small amount of each sample was transferred to a glass plate and mixed with isopropanol (96%) to promote evaporation of the aqueous phase. Analysis with the FTIR spectrometer requires a minimal amount of water in the samples, as this can interfere with the spectrum and would result in an unrealistic peak for the water content. Therefore, the samples were dried in the oven at 35 °C for about half an hour, until only a dry powder was left on the glass plate. This powder was scraped off of the plate, mixed with KBr, and grounded using a mortar and pestle. The sample cup was filled with this final mixture and placed in the spectrometer.

For each sample, the spectrum was collected by combining 64 integrated spectra, producing a spectral resolution of 4 $cm^{-1}$. The background noise was automatically removed from the sample spectra by the OMNIC control program and spectral analysis was done using FITYK-curve and peak fitting software. Before being able to use the peak measurements for calculations, the spectra had to be normalized to make sure that they all had the same ratio. Otherwise, a higher peak could also indicate a higher concentration of sample powder in comparison to the KBr during the FTIR analysis. The FTIR spectra were normalized using the $v_3PO_4$ peak at 1038-1041 $cm^{-1}$. The crystallinity of the samples was determined by using the full-width half maximum (FWHM) method, which measures the width of a spectral peak between two points on the y-axis that are at half the maximum amplitude of this peak. As a mineral becomes less crystalline, spectrum peaks become wider. Therefore, the inverse of the FWHM represents the mineral's crystallinity index. In the FTIR data, the $v_4PO_4$ peak was used to measure this crystallinity index.

### *V.II.b Raman spectroscopy*

The sample minerals were also analysed using a WITec UHTS Raman spectrometer. To prepare the samples for this analysis, they were taken out of the freezer and defrosted. A small amount of precipitate from each tube was spread out on a glass plate, which was left to air dry until all the visible water had evaporated and a dry powder was left. The glass plate was then placed in the sample chamber and an objective lens with a magnification of 50 times was used to find suitable crystals for spectrum collection. At least four spectra were taken of different crystals within each sample powder, using the green laser (532 nm).

The spectra were corrected for cosmic noise using the repair tool in the WITec Control Program 4.1 and cropped from 300 nm to 4000 nm. The background of each spectrum was removed using a shape size of 1000 and a noise factor of 0.15. After normalizing the Raman data to the $v_1PO_4$ peak around 957-960 $cm^{-1}$, further analysis and fitting of the spectra was done using the FITYK-curve and peak fitting software. The same $v_1PO_4$ peak was used to determine the crystallinity index of the samples.

## V.III Dissolution experiments

### *V.III.a Solution synthesis*

The dissolution experiments that were performed in this study used a solvent that was composed to mimic the fluid in the dissolution compartment of the osteoclast. As reported by Lu & Leng (2005), the chloride content of blood plasma is 103 mmol/L and Qin (2012) mentions a pH value of 4.5 in the resorption lacuna. Therefore, a sodium chloride solution with a molarity of 0.103 and a pH of 4.5 was synthesised. As we were also interested in the effect of pH on the dissolution process, another solution with a pH of 6.5 was prepared. To make sure that the pH remained constant for each sample during the experiments, a buffer was added to both solutions. The solution with pH 4.5 contained a 0.01 M sodium-acetate buffer. It was synthesised by dissolving 5.733 g sodium chloride (NaCl, provided by Merck) in 1000 mL of UHQ and adding a mixture of 0.334 mL acetic acid ($CH_3COOH$, provided by Peter Kraal) and 0.328 g sodium acetate ($CH_3COONa$, provided by Merck). The solution with pH 6.5 was buffered using an MES buffer, which is the common name for 2-(N-morpholino) ethanesulfonic acid ($C_6H_{13}NO_4S$, provided by Merck). This solution had a buffer strength of 0.01 M and was made by dissolving 5.623 g sodium chloride and 1.952 g MES in 1000 mL of UHQ. Then, sodium hydroxide (NaOH, provided by Merck) was added until the pH reached 6.5. The pH values of the final sodium chloride solutions were checked with the Consort C830 pH meter.

### *V.III.b AFM experiment and imaging*

#### Sample preparation

For a sample to be suitable for AFM analysis, the surface has to be relatively horizontal. It is also important that the particles do not move during scanning because this will interfere with the signal and result in a blurry image. In this study, the sample particles were mounted to a silicon wafer, which is a well-known substrate for AFM experiments as small particles are likely to stick to its surface. The silicon wafers were cleaned by ultrasonication in a layer of isopropanol for four minutes, after which they were dried with nitrogen gas. To make sure no organics were left on the surface, the wafers were placed under a UV-light with a wavelength of 253 nanometres for three minutes. In the meantime, the sample tubes intended for AFM analysis were defrosted and mixed by placing them on the Vortex-Genie 2 for ten seconds. Immediately after mixing, a pipette was used to transfer 5 µL from the sample tube to the silicon wafer, which was then sprayed with isopropanol until the sample solution was diluted enough to cover the surface with a fine layer of particles. The sides of the silicon wafer were tapped on the table to distribute the particles equally, but also to facilitate attachment of the particles to the wafer surface. Then, after waiting for 24 hours for the samples to dry, they were blasted with compressed air to get rid of any loose particles that might get stuck to the AFM tip during analysis. To see if the cleaning process changed the surface of the silicon wafers and what it looked like without addition of the sample, one silicon wafer was scanned before and after cleaning.

#### Imaging and analysis

To obtain images of the different sample minerals prior to dissolution, extra silicon wafers were prepared as described previously for the AFM sample preparation. Pictures of the samples were taken using a Leica DMLM Reflectance/Transmission Optical Microscope, which was set-up to be used with reflected light. Then, before starting the dissolution experiments, the silicon wafers were subjected to a test-scan. This gave insight on the ability of the AFM to scan the sample particles and also provided more detailed, high-magnification images of the sample minerals prior to dissolution. The silicon wafer was mounted onto a metal plate and placed onto the AFM sample holder. The microscope was used to find a suitable particle for analysis and after the laser was adjusted to obtain an optimum signal, the tip was brought down to the sample surface. The scanning type used during this study was the AFM contact mode and the Bruker Nanoscope v2.6.14 software was used to analyse the results.

For the dissolution experiment, the fluid cell was prepared and set-up along with a fluid pump. This pump was holding a 20 mL syringe filled with a sodium chloride solution, which had a pH of 4.5 and was prepared earlier. Initially, the pump was started at a rate of 0.5 mL/hour, which was turned down to 0.1 mL/hour after the fluid had filled the entire compartment. Then, the scanning process continued as described above, where the microscope was used to find a suitable particle, the laser was adjusted and the tip brought down to the sample surface. To ensure that the O-ring was safely attached and no fluid was leaking out of the fluid cell, the whole set-up was continuously checked during set-up and running of the experiment.

### *V.III.c Bulk dissolution experiment*

#### Set-up and preparation

Apart from the *in situ* AFM dissolution experiment, another dissolution experiment was carried out where the sample particles were dissolved in two different solutions (pH 4.5 and 6.5) and samples were taken at specific time-steps. To prepare for this experiment, the samples were defrosted and spread out onto glass plates, which were left to dry in the oven at 35 °C for about 3 hours. Once the powders had dried completely, each sample was scraped off of the glass plate and weighed. Before the main dissolution experiment, several smaller experiments took place. First, a small amount of each sample was dissolved in 1 M hydrochloric acid (HCl) to test the total amount of phosphate in the sample, and to see what sample to solution ratio resulted in measurable phosphate values. Also, two test-runs of the main experiment were carried out using only one sample, to make sure the experimental set-up was functioning correctly and to give an indication of the number of sampling moments that were needed to record the full dissolution process. For the first test-run, 6.5 mg of dried powder from sample CO3 was dissolved in 50 mL of the sodium chloride solution (pH of 4.5), which was prepared earlier. Samples were extracted every 10-15 minutes during 2 hours. The next test run was done in the same manner, only this time the solution with pH 6.5 was used. Then, the main experiment was done twice, dissolving all samples for a duration of 180 minutes, while taking samples of each solution after 5, 10, 20, 30, 45, 60, 75, 90, 120, 150 and 180 minutes.

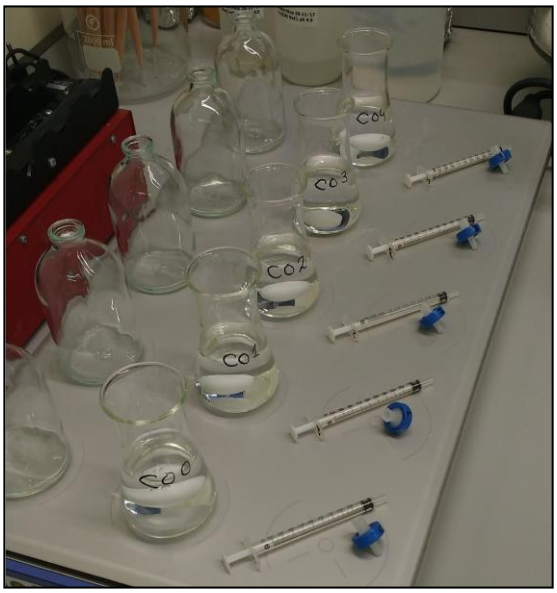


**Figure 4. Set-up of the bulk dissolution experiment. The septum bottles used to transfer the sodium chloride solution to the experiment are shown on the far left. In the middle row are the sample beakers containing the stirring bar, sample powder and sodium chloride solution. The syringes and filter used for sample extraction are on the right.**

### Experiment

The dissolution experiments started when 50 mL of the sodium chloride solution (pH 4.5 or 6.5) was added to a beaker containing a stirring bar and 6.5 mg of the dried sample powder. As it took about one minute to take one sample, the solutions were added to each beaker with two minutes between them, allowing enough time to take each sample while still ensuring an equal dissolution time. The first solution that was used to dissolve the powder had a pH of 4.5 and was buffered with a sodium acetate buffer. The second solution had a higher pH of 6.5 and was buffered using an MES buffer. All solutions were continuously stirred during the experiment at a speed of 250 RPM. For both the test-run and the first main experiment, 0.5 mL was extracted from the beaker using a 1 mL syringe. Then, any solid particles were removed from the solution by a small filter with a pore size of 0.2 µm (13 mm diameter). A different filter was used for every sample and the filters were cleaned in between sampling moments by rinsing them with UHQ once and pushing out the remaining water with an air-filled syringe. For the second experiment, 1 mL of solution was extracted and filtered with a big syringe filter with a pore size of 0.2 µm and a diameter of 21 mm. These filters were thrown away after use, as the cleaning method did not work as well as with the smaller filters and some water remained in the filter after cleaning.

## *V.III.d Colourimetric phosphate analysis*

The liquid samples that were collected during the bulk solution experiment were stored in 5 mL sample tubes for colourimetric analysis. The molybdenum blue method is based on the measurable colour change of the analyte (phosphate) after addition of a specific reagent (molybdate). The sample containing the phosphate is mixed with an acid molybdate ($Mo^{VI}$) solution, such as ammonium heptamolybdate ($(NH_4)_6Mo_7O_{24}$). This produces phosphomolybdate ($PMo_{12}O_{40}^{3-}$), which is reduced by the addition of ascorbic acid ($C_6H_8O_6$) and creates a blue coloured complex, $PMo_{12}O_{40}^{7-}$ (Barrows, 1985). The amount of this blue ion in the final solution corresponds directly to the amount of phosphate that was present in the original sample. Therefore, absorption of a solution can be used to determine the amount of phosphate that was released during dissolution of the sample powders.

| | $C_p$ (µM) | P stock (µl)[1] | Matrix (µl)[2] | Mixing reagent (µl)[3] | UHQ (µl)[4] | End volume (µl) |
|---|---|---|---|---|---|---|
| **1** | 0.0 | 0 | 25 | 800 | 1000 | 1825 |
| **2** | 0.5 | 10 | 25 | 800 | 990 | 1825 |
| **3** | 1.1 | 20 | 25 | 800 | 980 | 1825 |
| **4** | 2.7 | 50 | 25 | 800 | 950 | 1825 |
| **5** | 5.5 | 100 | 25 | 800 | 900 | 1825 |
| **6** | 8.2 | 150 | 25 | 800 | 850 | 1825 |
| **7** | 11.0 | 200 | 25 | 800 | 800 | 1825 |
| | | **Sample (µl)** | | **Mixing reagent (µl)[3]** | **UHQ (µl)[4]** | |
| | | 25 | | 800 | 1000 | 1825 |

**Table 2. Recipe for calibration series and sample measurements. [1] The P stock had a concentration of 100 µM and was provided by Helen King. [2] Comprises the solution used for the dissolution experiment. [3] Ahm: Ammonium heptamolybdate ((NH4)6Mo7O24). Made by adding 0.42g ascorbic acid per 100 mL molybdate solution (recipe given in Table 3). [4] UHQ: Volume of ultra-high quality water needed to reach an equal end volume in each cuvette.**

| | Stock | End volume (mL) | Regular samples |
|---|---|---|---|
| **1** | Ammonium heptamolybdate (Ahm) | 500 | 2.4 g |
| **2** | Sulphuric acid ($H_2SO_4$) | | 28 mL |
| **3** | Potassium antimony oxide tartrate hemihydrate ($C_8H_6K_2O_{13}Sb_2$) | | 0.0565 g |
| **4** | UHQ | | Dilute to 500 mL |

**Table 3. Molybdate solution for samples (stored in the dark at 4°C no longer than 2 months).**

The absorption is measured using a UVmini-1240 UV-VIS spectrophotometer and a wavelength of 880 nm. To be able to convert the absorbance values into phosphate concentrations, a calibration curve is needed. This curve was obtained by measuring the absorbance of a series of semi-micro cuvettes (2000 µL) with increasing amounts of phosphate. Specific amounts of UHQ, mixing reagent, and either sample or matrix were added to each cuvette (Table 2). Then, the cuvettes were closed and inverted 2 times to homogenise the solution. As the colour develops within 10 minutes and starts to fade around 100 minutes after preparation, the absorbance was measured after 30 minutes.

To calculate the amount of phosphate that relates to the absorbance of the samples taken during the dissolution experiments, a calibration curve was needed. This curve was made by measuring the absorbance of a series of samples with a known phosphate concentration and fitting a trend line to the results. The recipe for the calibration series is given in Table 2 and the resulting trend line should have an equation in the form of y = ax – b, where the y-value represents the absorbance and x depicts the phosphate concentration in µM. This formula was used to calculate the amount of phosphate in the samples.

# VI. RESULTS

## VI.I pH during sample synthesis

Before mixing the solutions from which the samples were going to precipitate, the initial pH value of each solution was measured. The calcium chloride solution that was used for all samples had a pH of 8.9, while the carbonate-phosphate solution varied between 9.1 (sample CO0) and 11.0-10.9 (samples CO1-CO4). Figure 5 displays the changes in pH that occurred after mixing the two solutions. As can be seen here, sample CO0 displayed a significant drop in pH from 6.00 to 5.17 during the first 5 minutes. The pH continued to decrease during the rest of the experiment, reaching 5.08 after 60 minutes. About one minute after mixing the solutions, samples CO1, CO2, CO3 and CO4 had a pH of 10.13, 10.48, 1.66 and 10.68, respectively. These values dropped slightly during the rest of the experiment and reached a pH of 9.99, 10.40, 10.60 and 10.64 after 60 minutes. This shows that the overall pH values increased with increasing sample number, while the change in pH decreased.

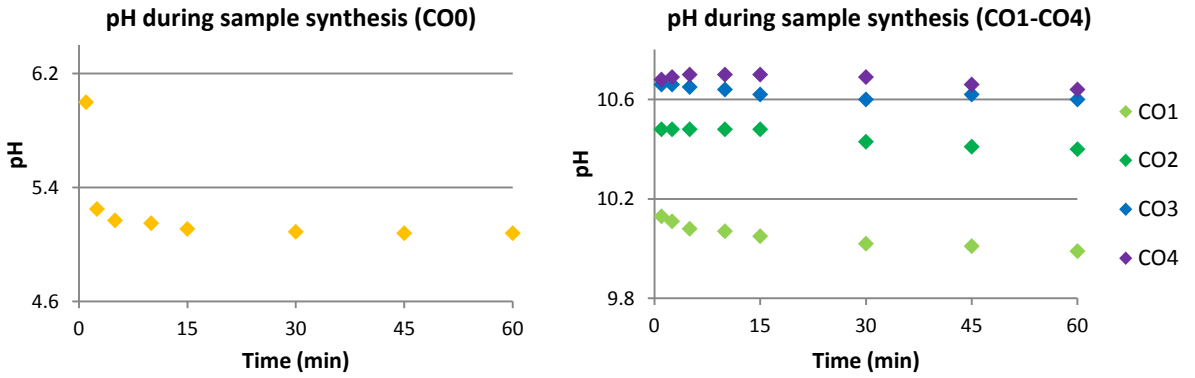


Figure 5. pH change of solutions during sample synthesis.

## VI.II Visual observations

### Sample synthesis

During synthesis of the samples, all solutions instantly turned white and cloudy after mixing the calcium solution and the carbonate-phosphate solution, which remained this way throughout the rest of the synthesis process. When the septum bottles containing the sample solutions were taken from the stirring plate for sampling, the suspensions separated into a layer of precipitate which was overlain by a layer of clear solution (the supernatant). No differences were observed between the samples after they were centrifuged and the precipitate was separated from the supernatant. However, when the samples were dried in preparation of the bulk dissolution experiment, this revealed that the powder from sample CO0 was very fine and had a glossy finish. The other powders were slightly more coarse and dull in appearance.

### Leica images

As can be seen in Figure 6, the Leica microscope pictures show a clear difference between CO0 and the other samples. The particles of this non-carbonated sample are fairly consistent in size and shape. The minerals are very thin and rectangular with rounded edges, where one side is often narrower than the other. The long particle side is between 50 and 70 µm long, while some very small particles (<1 µm) are also present. The light from the microscope is reflected by the flat surface of the minerals, causing them to have different colours, depending on the way the light hits the surface. This can be seen very well in Figure 6a, which also shows how the particles are stacked upon each other. Underlying particles can even be seen through the translucent, overlying minerals.

This translucent characteristic is not seen in the other samples, where the minerals are mostly equidimensional and lack the flat, reflecting surfaces. Some particles found in sample CO1 and CO2 do show a flat surface, as can be seen in Figure 6b and Figure 6c. However, most particles have a rough shape, which makes it difficult to focus the microscope and obtain a clear image. In general, the carbonated sample minerals are relatively similar in shape, and three different types can be recognized. Some minerals have a flat surface when viewed from above, and five to six well-developed sides that are roughly the same length, forming a pentagon or hexagon. Other minerals also have a flat surface when seen from above, but have four or five sides and resemble a diamond or kite shape. The third and last type comprises the particles with various shapes that are more difficult to define, as they have multiple corners and un-developed edges. The overall sizes of the minerals are between 10 and 80 µm, but there does seem to be an increase of smaller particles in sample CO4, compared to the lower sample numbers.

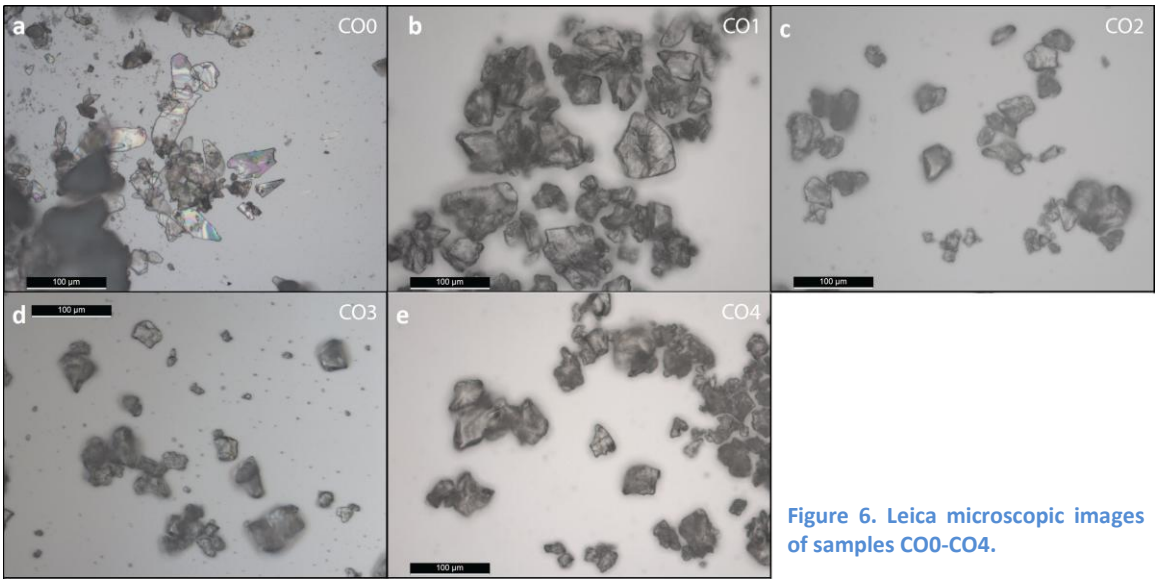


Figure 6. Leica microscopic images of samples CO0-CO4.

### AFM images

Before the dissolution experiment, the silicon wafers that were prepared earlier were subjected to a test-scan. The resulting images are displayed in Figure 7, which shows the big morphological differences between CO0 and the other samples. The minerals in CO0 are rectangular and very thin, as was observed in the Leica images as well. The particles in samples CO1 to CO4 have a triangular to kite-like shape, with a flat surface when viewed from above. They occur in aggregates (Figure 7b), on their own (Figure 7h) or can be found as a layer covering the silicon wafer surface (Figure 7g). The size of the individual minerals that are imaged in samples CO1-CO4 is between 1 and 2 µm, although the aggregates can be up to 5 µm. Bigger particles and aggregates were also present, but they didn't stick to the silicon wafer surface very well and were moved around by the tip of the AFM during the scanning process, resulting in unclear images. When comparing the images of samples CO1, CO2, CO3 and CO4, it seems that the minerals in CO1 have relatively smooth surfaces compared to the higher numbered samples. These smooth surfaces can still be recognized in sample CO2, but are more difficult to find in sample CO3 and CO4. The small, individual minerals can still be distinguished within the aggregates, but are noticeably less clear.

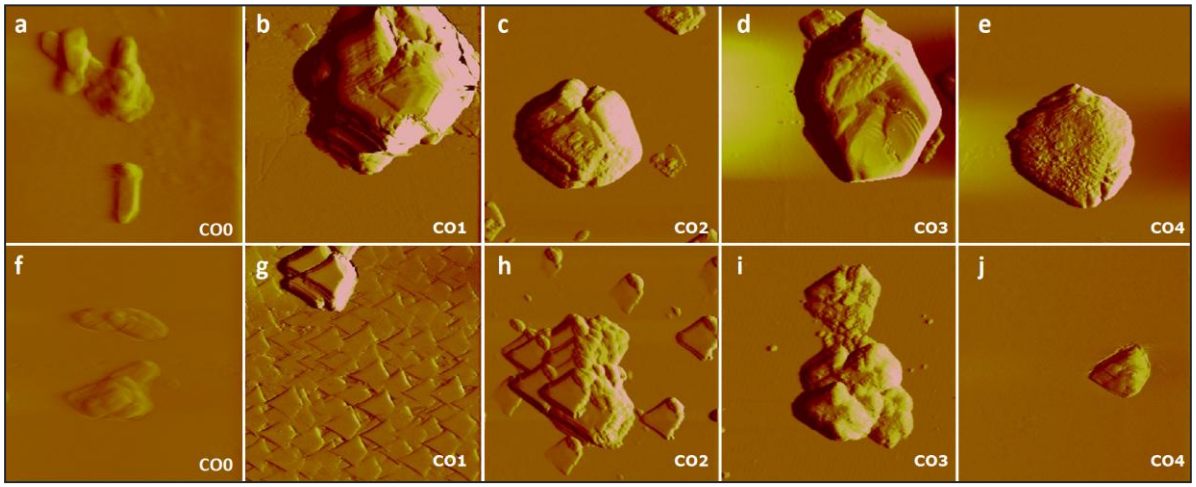


Figure 7. AFM pictures from samples CO0-CO4. Picture width is 5 µm, except for 7a (top left) which is 4 µm wide.

## VI.III Chemical analysis

### *VI.III.a Spectroscopic characterization*

### FTIR data

The spectra collected from FTIR spectroscopy shows similar peak positions and shapes for all samples, except for the spectrum of sample CO0, to which no carbonate was added (Figure 8). The lower end of the wavenumber spectrum displays two peaks that are consistently seen in all spectra between 520 and 640 $cm^{-1}$. According to Rehman & Bonfield (1997), they can both be attributed to the $v_4$ vibrational stretch of phosphate. The first peak in this region shifts to higher wavenumbers between 561 and 571 $cm^{-1}$ for sample CO0 and sample CO4, respectively, and has a shoulder at ~585 $cm^{-1}$, which is slightly shifted to 575 $cm^{-1}$ for CO0. The other peak in this region occurs at 601 $cm^{-1}$ for CO0 and around 605 $cm^{-1}$ for the carbonated samples. Although the shapes are roughly the same, the width of this second peak is significantly narrower for sample CO0. Additionally, sample CO0 shows peaks at 528, 628 and 645 $cm^{-1}$, where the latter occurs as a weak shoulder. The peak at 628 is related to the $OH^-$ stretch (Boudia, 2018). The next peak that is present in all spectra occurs around 872 $cm^{-1}$. This narrow band represents the $v_2CO_3$ out-of-plane bending mode for the carbonated samples (Fleet, 2009) and the $HPO_4$ mode for CO0 (Drouet, 2013). Another peak that is correlated with the presence of $HPO_4^{2-}$ ions occurs at 914 $cm^{-1}$ in sample CO0. It is absent in the other samples.

A large peak is seen in all spectra between 1000 and 1100 $cm^{-1}$. This region is associated with the $v_3$ asymmetric stretch of phosphate (Rehman & Bonfield, 1997; Fleet, 2009). The carbonated samples have a shoulder peak around ~963 $cm^{-1}$, which is slightly shifted to 965 $cm^{-1}$ for the sample without carbonate, but both can be attributed to the $v_1$ stretch of phosphate (Rehman & Bonfield, 1997). The main peak is at its maximum between 1035 and 1048 $cm^{-1}$ for the carbonated samples, but shows a different, more complex shape for sample CO0, as this spectrum reaches a maximum height at 1029 $cm^{-1}$. Also, sample CO0 has three extra peaks at 1080, 1123 and 1209 $cm^{-1}$ and three additional shoulders at 988, 1040 and 1056 $cm^{-1}$. Furthermore, all spectra have a shoulder between 1096 and 1099 $cm^{-1}$, which progressively becomes weaker when more carbonate is added to the sample. According to Rehman & Bonfield (1997), the $v_3$ asymmetric stretch of phosphate results in three individual peaks in laboratory-produced hydroxyapatite (HA) crystals at 1056, 1085 and 1096 $cm^{-1}$, which would explain the peaks observed in sample CO0 at 1056, 1080 and 1096 $cm^{-1}$. However, in carbonated apatite (CA), this $v_3$ mode is expressed by one intense band at 1046 $cm^{-1}$. This corresponds to the main peak that is displayed between 1035 and 1048 $cm^{-1}$ for the carbonated samples and could also correspond to the shoulder peak in CO0. Rehman & Bonfield (1997) also mention that the $v_1CO_3$ mode can be obscured by the intense $v_3PO_4$ stretching band.

The peaks that occur around ~1416 and ~1472 $cm^{-1}$ are related to the $v_3$ asymmetric stretch of carbonate (Rehman & Bonfield, 1997). They are only found in the spectra of the carbonated samples and are absent in sample CO0. In the region between 1600 and 1800 $cm^{-1}$, all carbonated and non-carbonated samples show a peak and a shoulder. There are, however, differences in peak location and shape. Sample CO0 displays a narrow peak at 1649 $cm^{-1}$ with a shoulder at 1725 $cm^{-1}$, while the peaks seen in the carbonated samples are both wider and taller. They are thought to correspond to the $v_3$ mode of carbonate (Rehman & Bonfield, 1997). Their peak locations vary between 1642 $cm^{-1}$ for sample CO1 and ~1650 $cm^{-1}$ for samples CO2, CO3, and CO4. The shoulder to this peak progressively becomes stronger from sample CO1 to CO4 and is located around ~1760 $cm^{-1}$ for CO1, CO2 and CO3, and at 1765 $cm^{-1}$ for CO4.

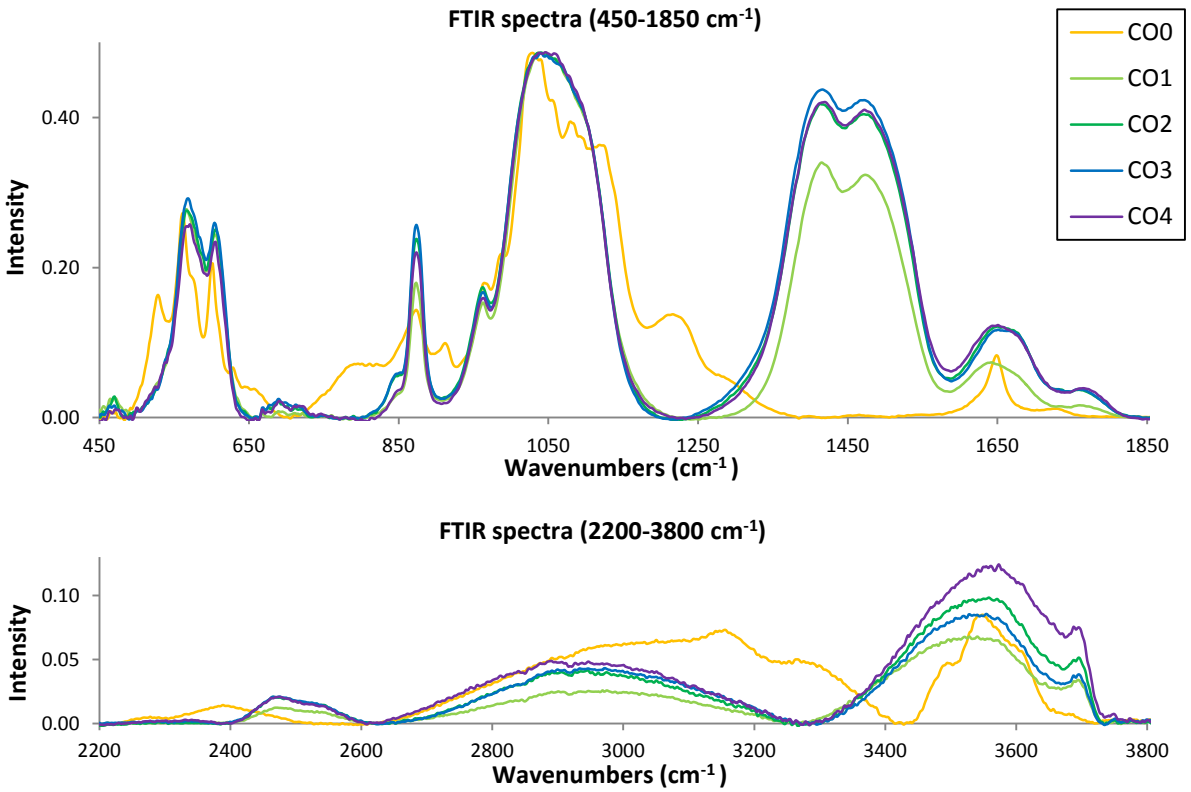


Figure 8. FTIR spectra of all samples. Spectra are normalized for the peak at 1038-1041 $cm^{-1}$.

In the higher end of the spectrum, two weak peaks occur at 1981-1994 and 2466-2478 $cm^{-1}$ in the carbonated spectra, with a weak to very weak shoulder around ~2524-2532 $cm^{-1}$. Only one peak is displayed in sample CO0 in this of the spectrum, located at 2390 $cm^{-1}$. Finally, the peaks that occur in the spectrum range over 2800 $cm^{-1}$ are attributed to the stretch of hydroxyl groups, due to the presence of water in the sample and $H_2O$ in the crystal structure (Rehman & Bonfield, 1997).

## Raman data

The Raman spectroscopic data showed similar results to what was previously described for the FTIR data. The peaks in the various carbonated samples occurred at similar locations and only minor differences were observed in their peak width and height. Sample CO0 displayed peaks at locations where no other peaks were present for the other samples. The first peak in the lower end of the spectrum occurs around 413 $cm^{-1}$ for sample CO0 and around 430 $cm^{-1}$ for the other samples. Both can be attributed to the $v_2PO_4$ mode (Penel, 1998; Khan, 2013). Other peaks that occur in all samples can be found at 585 and ~611 $cm^{-1}$. They are related to the $v_4PO_4$ mode, according to Penel (1998), Crane (2006) and Khan (2013). The same authors mention that the intense peak that is present in all samples at 958 $cm^{-1}$ can be attributed to the $v_1PO_4$ mode. CO0 has another intense peak at 983, and some smaller additional peaks at 520 and 873 $cm^{-1}$. According to Crane (2006), these peaks are mostly related to the $HPO_4$ mode. Next, the carbonated samples display an intense peak with varying height around 1070 $cm^{-1}$ which can be attributed to the B-type $v_1CO_3$ mode (Penel, 1998; Khan, 2013). Sample CO0 does not have one big peak in this region but instead displays three weaker peaks at 1052, 1081 and 1127 $cm^{-1}$. Lastly, the peaks in the higher end of the spectrum (3000-3700 $cm^{-1}$) can be attributed to the $OH^-$ stretching mode (Khan, 2013). The peaks vary between 3427 and 3436 $cm^{-1}$ for the carbonated samples, while several smaller peaks are present at 3265, 3473 and 3535 $cm^{-1}$ for sample CO0.

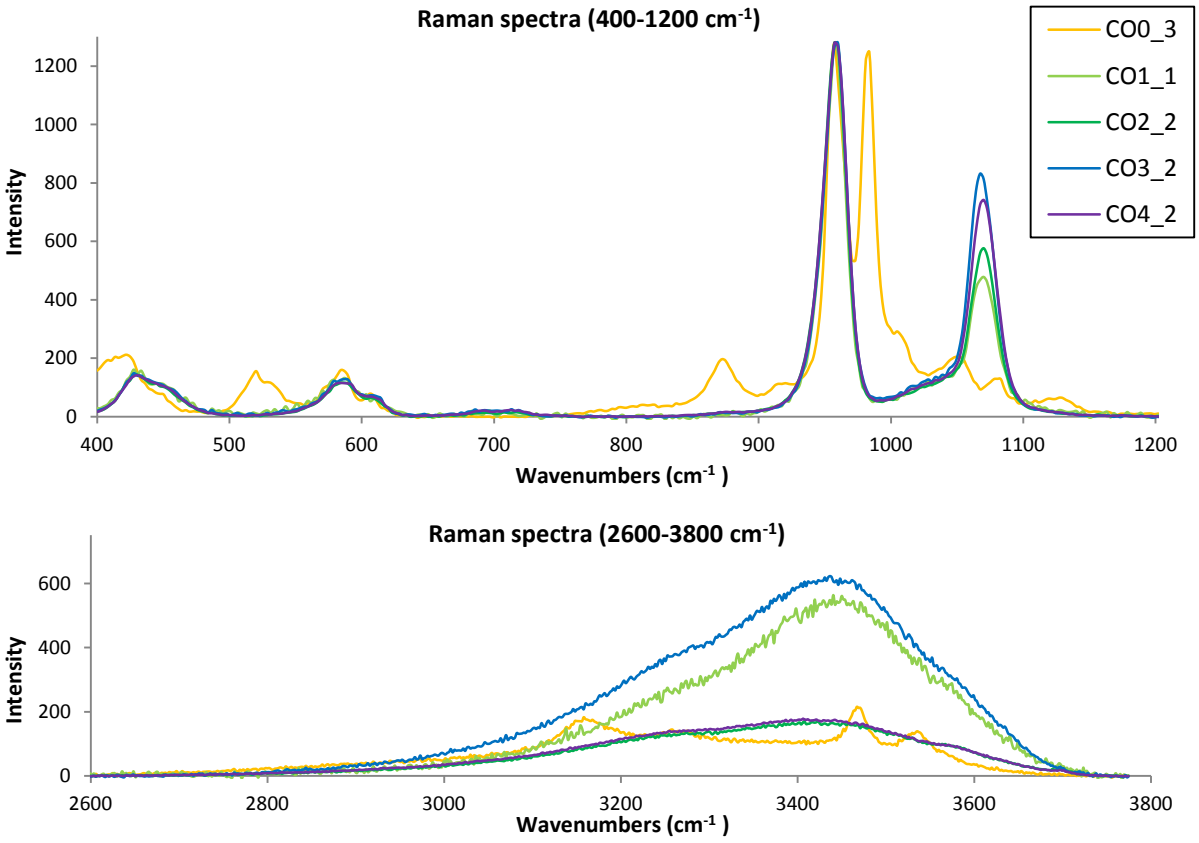


Figure 9. Raman spectra of all samples. Spectra are normalized for the peak at 956-960 $cm^{-1}$.

| CO0 | CO1 | CO2 | CO3 | CO4 | Peak assignment |
|---|---|---|---|---|---|
| 528 | - | - | - | - | $HPO_4$ bending OCP [3] |
| - | - | - | - | 566s | |
| 561 | 566 | 567 | 568 | 571 | $v_4PO_4$ CA [1,3], $HPO_4$ bending OCP [3] |
| 575s | 583s | 586s | 585s | 585s | $HPO_4$ bending OCP [3] |
| 601 | 605 | 605 | 604 | 605 | $v_4PO_4$ CA [1,3] |
| 628 | - | - | - | - | $OH^-$ stretch [3] |
| 645ws | - | - | - | - | |
| 791s | | 845ws | 847ws | 848ws | |
| 874 | 872 | 872 | 872 | 872 | $HPO_4$ stretch OCP [3], $v_2CO_3$ [1,2,4] |
| 914 | - | - | - | - | $HPO_4$ stretch OCP [3,4] |
| 965s | 963s | 962s | 963s | 963s | $v_1PO_4$ CA + HA [1,3] |
| 988s | - | - | - | - | |
| 1029 | - | - | - | - | $v_3PO_4$ HA [1,3] |
| 1040s | 1035-1048 | 1034-1042 | 1038-1042 | 1046-1048 | $v_3PO_4$ HA [1,3] |
| 1056s | - | - | - | - | $v_3PO_4$ HA [1,3] |
| 1080 | - | - | - | - | $v_3PO_4$ HA [1,3] |
| 1096s | 1099s | 1099s | 1097ws | 1097vws | $v_3$ $PO_4$ HA [1] |
| 1123 | - | - | - | - | |
| 1209 | - | - | - | - | $HPO_4$ in-plane-bending [3,4] |
| - | 1416 | 1415 | 1415 | 1419 | $v_3CO_3$ HA [1,2] |
| - | 1473 | 1472 | 1471 | 1472 | $v_3$ $CO_3$ CA [1,2] |
| 1649 | 1642 | 1651 | 1650 | 1651 | $v_3$ $CO_3$ CA+HA [1,2] |
| 1725s | 1761s | 1759s | 1759s | 1765s | |
| - | 1984-1994w | 1981-1998w | 1988w | 1986w | |
| 2390w | 2466-2477w | 2466w | 2466w | 2469-2478w | |
| | 2532vws | 2524ws | 2531vws | 2524ws | |
| >2800 | >2800 | >2800 | >2800 | >2800 | |

**Table 4. Peak positions ($cm^{-1}$) of the FTIR spectra collected (determined without deconvolution), where w=weak, s=shoulder, ws=weak shoulder, HA=hydroxyapatite, CA= carbonated apatite, OCP = octacalcium phosphate. Assignments are based on findings of [1] Rehman & Bonfield, 1997; [2] Fleet, 2009; [3] Boudia, 2018 and Drouet, 2013 [4].**

| CO0 | CO1 | CO2 | CO3 | CO4 | Peak assignment |
|---|---|---|---|---|---|
| 413w | 429w | 429w | 430w | 430w | $v_2PO_4$ [1,3] |
| 520 | - | - | - | - | |
| 583w | 585w | 586w | 585w | 587w | $v_4PO_4$ [1,2,3] |
| 607ws | 613ws | 611ws | 612ws | 612ws | $v_4PO_4$ [1,3] |
| - | - | - | 693vw | 694vw | |
| - | 703vw | 705vw | 712vw | 712vw | |
| 873w | - | - | - | - | $HPO_4$ [2], C-C stretching [3] |
| 957 | 958 | 958 | 958 | 958 | $v_1PO_4$ [1,2,3] |
| 983 | - | - | - | - | $HPO_4$ or $v_1PO_4$ [2] |
| - | 1031ws | 1027ws | 1027ws | 1025ws | $v_3PO_4$ [1,3] |
| 1052w | - | - | - | - | $v_3PO_4$ [3] |
| 1081w | 1069 | 1070 | 1068 | 1070 | B-type $v_1CO_3$ [1,3] |
| 1127w | - | - | - | - | |
| 3160 | - | - | - | - | |
| 3265 | - | - | 3255s | 3250s | |
| 3473 | 3437 | 3427 | 3440 | 3436 | OH stretching [3] |
| 3535 | - | - | - | - | OH stretching [3] |

**Table 5. Peak positions ($cm^{-1}$) of the collected Raman spectra (determined without deconvolution), where w=weak, s=shoulder, and ws=weak shoulder. Assignments are based on findings of [1] Penel, 1998; [2] Crane, 2006 and Khan, 2013 [3].**

### *VI.III.b Carbonate type and content*

The way carbonate is incorporated into the apatite crystal lattice can be characterized using FTIR spectroscopy (Ren, 2013). The Raman spectroscopy data can, in turn, be used to determine the total amount of B-type substitution, where phosphate is replaced by carbonate. It can, however, not distinguish between adsorbed or incorporated $CO_3^{2-}$ (De Groot, 2017). Therefore, comparing the information from both FTIR and Raman analyses will give the best possible answer to how carbonate incorporation took place during sample synthesis. Since both the FTIR and Raman data showed no indication of the presence of carbonate in sample CO0, the calculations of carbonate type and content are not included for this sample. However, sample CO0 is included in some of the figures to make it easier to compare the samples and recognize their relationships.

Figure 10a plots the carbonate content versus the amount of carbonate that was added to the carbonate-phosphate solution during synthesis of the samples. Here, the carbonate content represents the total amount of carbonate that was incorporated into each sample, which was obtained by measuring the $v_2CO_3/v_3PO_4$ ratio of the FTIR spectra. The data in the figure shows a positive correlation between the incorporated carbonate and the initially added carbonate for all samples, with an exception for sample CO4, which has a slightly lower carbonate content than CO2. The lines in Figure 10b each represent a different way in which the carbonate was incorporated into the crystal lattice. These values are obtained by deconvolution of the $v_2CO_3$ region in the FTIR spectra. The area of either the peak at ~866, ~872 or ~878 $cm^{-1}$ was divided by the total area of the $v_2CO_3$ peak to obtain the relative amounts of labile, A-type or B-type substitution, respectively (Delgado-López, 2012). An example of the deconvolution of the $v_2CO_3$ region of sample CO4 is shown in Figure 10c, which shows that the peak at ~866 $cm^{-1}$ is relatively small compared to the other peaks. However, it is clearly present and can be seen in Figure 10b as well, where sample CO4 is the only sample with a significant amount of labile carbonate, while it is almost negligible for the other samples. The A-type substitution shows a similar, rising trend to the labile type, but has higher overall values. Also, there is a slightly bigger increase in A-type carbonate content between CO2 and CO3. The B-type substitution is dominant in all samples but shows a relative decrease in intensity from CO1-CO4. This gradually decreasing trend corresponds to the increase in both labile and A-type substitution between samples CO2, CO3, and CO4.

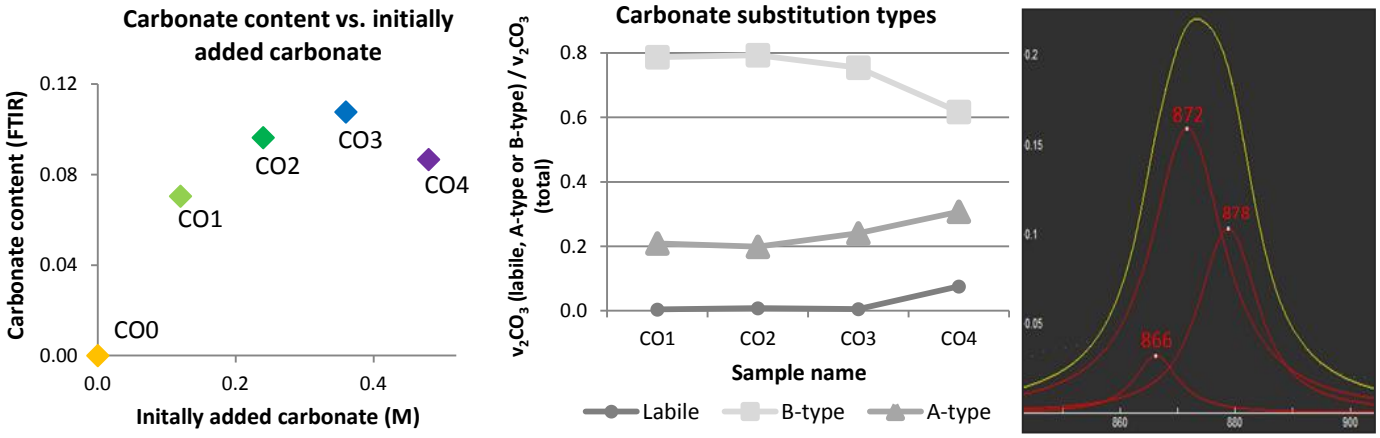


**Figure 10a (left): Initially added carbonate (M) versus the carbonate content as determined from the FTIR data. Figure 10b (middle): Relative intensity of carbonate substitution types (A-type, B-type and labile) for each sample. Figure 10c (right): Example of deconvolution of the v2CO3 region in the FTIR spectrum of sample CO4, where the peaks at 866, 872 and 878 $cm^{-1}$ represent the amount of labile, A-type and B-type carbonate substitution for this sample, respectively.**

Figure 11a displays the B-type carbonate as obtained from the Raman data, by measuring the area ratio of the B-type, $v_1CO_3$ and $v_3PO_4$ peak over the $v_1PO_4$ peak (Penel, 1998). According to this data, the B-type carbonate content is lowest for CO1 and highest for CO3, with CO2 and CO4 lying in between. The total carbonate content as calculated from the FTIR data is plotted against the B-type carbonate as obtained from the Raman data in Figure 11b. This graph shows a positive correlation between these first three samples and a deviant value for CO4. Finally, an overall similarity is observed between the B-type carbonate content from the Raman data (Figure 11a) and the total carbonate content (Figure 10a). Both graphs show an overall increase in (B-type) carbonate content with increasing sample number, reaching a maximum value for CO3 and a slight decrease between samples CO3 and CO4.

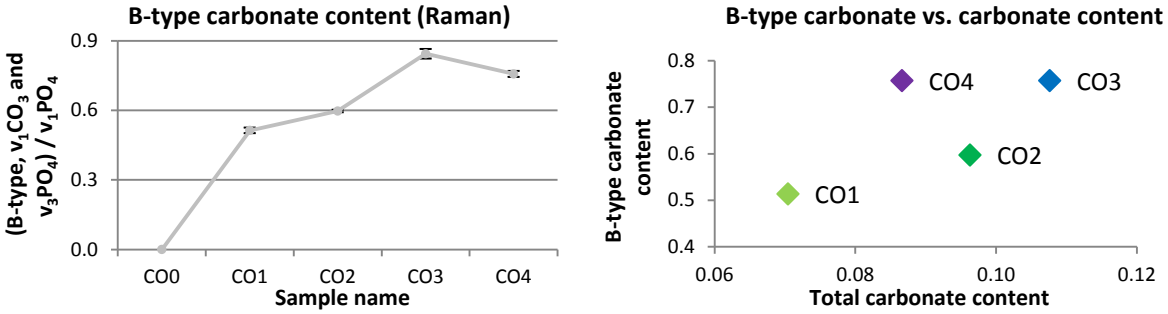


**Figure 11a (left): B-type carbonate, calculated from Raman data. Error bars display variation in values, as multiple spectra of each sample were taken. Figure 11b (right): B-type substitution (Raman) versus total carbonate content (FTIR).**

### *VI.III.c Crystallinity*

The crystallinity index of all samples was determined by taking the inverted FWHM of the $v_1PO_4$ peak that was seen consistently in the Raman spectra between 957 and 960 $cm^{-1}$. The same was done for the $v_4PO_4$ peak that appeared around 605 $cm^{-1}$ in the FTIR spectra. As displayed in Figure 12, the results are very similar. Although the exact numbers are different, the same trend can be observed, as the crystallinity decreases from sample CO0 to CO4. Although this decrease is the biggest between CO0, CO1, and CO2, a slight decrease is still visible between CO2, CO3 and CO4.

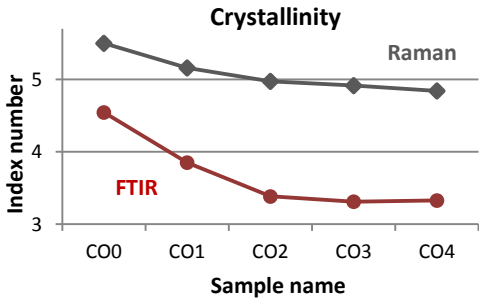


**Figure 12. Crystallinity index for all samples, calculated using the inverse of the FWHM value from either the $v_1PO_4$ peak at ~957 $cm^{-1}$ in the Raman data (grey line) or the $v_4PO_4$ peak at ~605 $cm^{-1}$ in the FTIR data (red line).**

## VI.IV Solubility

### AFM dissolution experiment

The AFM dissolution experiment did not work as well as expected. The set-up was very sensitive to movement, making it difficult to move the AFM tip around and find a stable particle which could be imaged. Many particles did not remain stuck to the surface when the solution was added. When they did, they often started to move during scanning, resulting in a blurred image. Other problems that occurred were leaks on the side of the O-ring and air bubbles within the system. On one occasion, a particle was scanned for 10 minutes before a small air bubble appeared and the experiment had to be ceased. During this time, no clear signs of dissolution were witnessed. Therefore it was decided not to continue with the dissolution experiments using the atomic force microscope method.

### *VI.IV.a Bulk dissolution experiment*

The results from the test-runs that were performed before the main dissolution experiment are shown in Figure 13. When measuring the phosphate levels of the samples that were taken during the first test-run, which used a sodium chloride solution with pH 4.5, all values were roughly the same (Figure 13a). For the second test-run, a sodium chloride solution with pH 6.5 was used. As can be seen in Figure 13b, the data points from this experiment form a clear trend where the absorbance of the samples increases significantly during the first 60 minutes. After this, the increase in absorbance stagnates and continues to rise at a slower rate. As the sample seemed to dissolve slower in the solution with pH 6.5 and this allowed for better determination of dissolution rates for the different samples, it was decided to continue the further experiments using the solution with this pH.

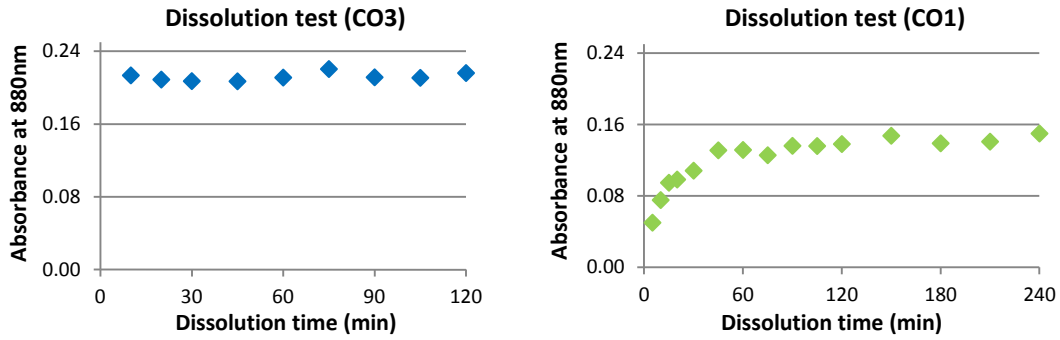


**Figure 13a (left): Results of the dissolution test with sample CO3 and a NaCl solution with pH 4.5. Figure 13b (right): Results of the dissolution test with sample CO1 and a NaCl solution with pH 6.5.**

The main bulk dissolution experiment was performed two times, using a sodium chloride solution with a pH of 6.5. Afterwards, the phosphate concentrations of the extracted samples were calculated by using the calibration curve shown in Figure 15, where the equation of the trend line was y = 0.0222x - 0.0015. The resulting phosphate concentrations are displayed in Figure 15, where the data points represent the mean value of the results at that specific time step. The lines show the trend line to these points, based on a logarithmic equation. The figure shows that CO0 has significantly higher concentrations than the other (carbonated) samples. It also experiences a faster increase during the first 15 minutes, along with sample CO3. The other samples CO1, CO2, and CO4 have lower initial values, but the phosphate concentration seems to increase for a longer time, even after concentration increase in CO0 and CO3 has stagnated.

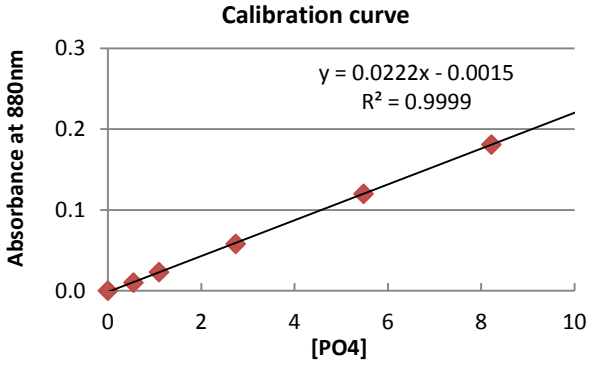


**Figure 14. Calibration curve of the spectrometer used to measure the samples from the dissolution experiment. The trend line equation was used to convert absorbance to phosphate concentration.**

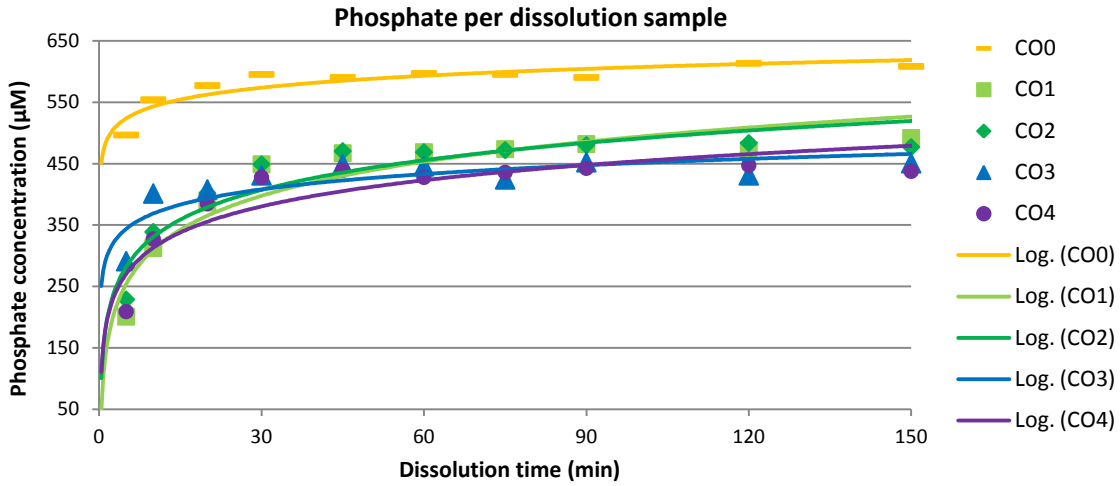


Figure 15. Phosphate concentration in µM per sample, over time.

The differences in dissolution between CO0 and CO3 and the other samples is even more noticeable when the release rate is expressed per time period (Table 6). The amount of phosphate released during the first 10 minutes is significantly higher for CO0 and CO3 (55.4 and 40.1 µMol/min) than for the other samples (~31-34 µMol/min), while during the next 20 minutes, CO1, CO2, and CO4 show the highest release rates (6.6, 5.3 and 4.8 µMol/min, respectively). CO0 and CO3 have much lower rates of 1.8 and 1.2 µMol/min. During the rest of the experiment, the values remain relatively stable with a maximum release rate difference between samples of 0.7 µMol/min. This confirms the earlier observation that CO0 and CO3 have the fasted release of phosphate right at the start of the experiment, after which the release rates quickly drop and stagnate. Sample CO1, CO2 and CO4 however, show a more gradual phosphate release, after which the rates go down.

| | Time (minutes) | | | | | |
|---|---|---|---|---|---|---|
| | **0-10** | **10-30** | **30-60** | **60-90** | **90-120** | |
| **CO0** | 55.4 | 1.8 | -0.1 | -0.4 | 0.3 | **Phosphate release rate (µMol/min)** |
| **CO1** | 31.2 | 6.6 | 0.5 | 0.3 | -0.2 | |
| **CO2** | 33.9 | 5.3 | 0.5 | 0.2 | 0.0 | |
| **CO3** | 40.1 | 1.2 | 0.3 | 0.1 | -0.4 | |
| **CO4** | 32.7 | 4.8 | -0.2 | 0.3 | 0.0 | |

Table 6. Amount of phosphate released per sample, per time period (µMol/min). The highlighted numbers show the highest release rates for that specific time period.

## Morphological and mineralogical changes

After 60 minutes of dissolution, extra samples were taken and prepared for AFM analysis. The resulting images (Figure 16) show mostly oval particles of similar sizes. Some subhedral, pentagonal to hexagonal particles can be recognized in sample CO3 and CO4, but they are very rare and not well developed. Analysis of these particles by Raman spectroscopy did not always result in clear spectra, due to the strong signal of the silicon wafer on which they were precipitated. The intensity of the laser proved to be another problem, as some particles disintegrated within seconds after the laser was turned on. This could indicate that these solid particles were highly hydrated and quickly evaporated by the heat of the laser. Despite these difficulties, some clear spectra were obtained. They are shown in Figure 17, along with a spectrum of the silicon wafer surface for reference. As this spectrum shows as well, the most characteristic feature of silicon is the intense peak at 522 $cm^{-1}$, along with the broader band between 946 and 978 $cm^{-1}$ and the small peak around 305 $cm^{-1}$ (RRUFF, 2018; Uchinokura, 1972).

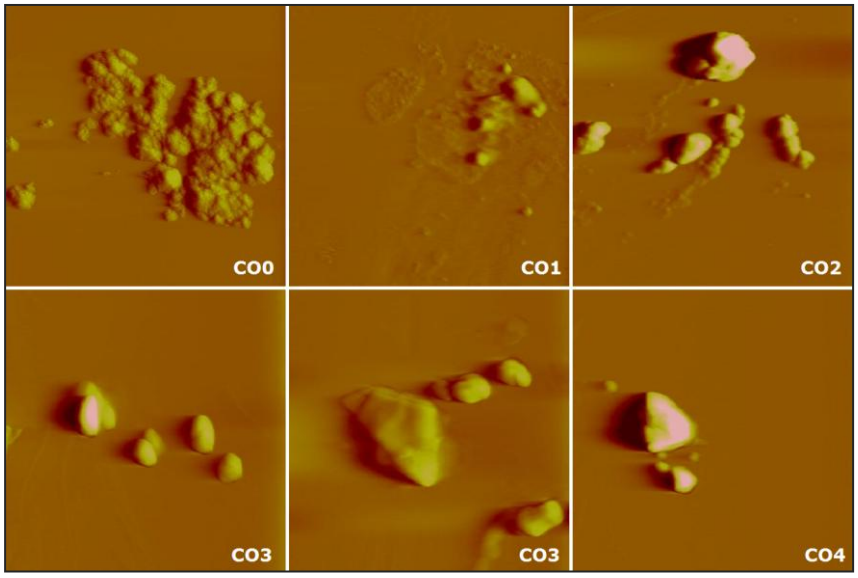


Figure 16. AFM pictures of samples CO0-CO4 after 60 minutes of dissolution. Images are 5 µm wide.

The other peaks in the spectrum are mostly related to molecular vibrations of phosphate and carbonate. An intense band caused by the $v_1PO_4$ stretch occurs at 961 $cm^{-1}$ in all samples, while the weaker band that is present in samples CO0 and CO1 at 432 $cm^{-1}$ represents the $v_2PO_4$ bending mode (Penel, 1998; Khan, 2013). These samples also exhibit a peak around 587 $cm^{-1}$, representing the $v_4PO_4$ bending character. The $v_3PO_4$ mode can be recognized by the band between 1032 and 1044 $cm^{-1}$ and is observed in samples CO3 and CO4. The relatively strong peak at 1071 $cm^{-1}$ in samples CO1, CO2, CO3 and CO4 is absent in CO0 and can be attributed to the $v_1CO_3$ mode (Penel, 1998). Two spectra for sample CO4 display a strong band at 1004 $cm^{-1}$, which can be attributed to the $v_3HPO_4$ mode (Penel, 1998; Khan, 2013) and is not found in any of the other spectra. The peaks in the higher end of the spectra (2800-3100 $cm^{-1}$) are mostly thought to represent the bending of C-H bonds (Khan, 2013). Along with some smaller bands, two distinct strong peaks around 2908 and 2966 $cm^{-1}$ are present in this region for all samples. Finally, samples CO3 and CO4 display two peaks at 1200 and 1311 $cm^{-1}$ that could possibly be related to the presence of Amide III (Khan, 2013). Some signs of Amide I molecules are also observed at 1605 and 1665 $cm^{-1}$, but these are only found in sample CO4.

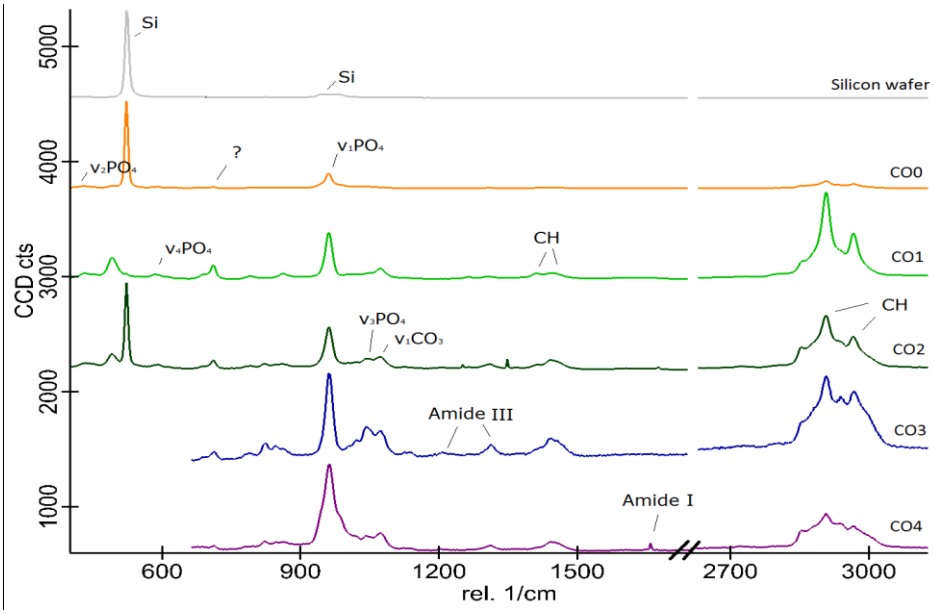


Figure 17. Raman data of the samples after being dissolved in a buffered 0.1 M NaCl solution with pH 6.5 for 60 minutes. A spectrum of the silicon wafer on which the particles were deposited is included for reference.

# VII. DISCUSSION

## VII.I Mineralogy

### Apatite formation in the absence of carbonate

The images taken with the camera of the Leica microscope (Figure 6) show a clear morphological difference between CO0 and the other samples. The characteristic minerals of sample CO0 are thin, platy and well-developed, which is in agreement with the high crystallinity index calculated from both the Raman and FTIR data (Figure 12). Considering that no carbonate was added during synthesis of this sample, it was expected that it would be most similar to the pure form of hydroxyapatite ($Ca_{10}(PO_4)_6(OH)_2$). The typical morphology of synthetic apatite varies with composition and experimental conditions, but it generally consists of plate- or petal-like minerals (Drouet, 2013; Sader, 2013). However, the presence of such minerals does not always indicate the formation of hydroxyapatite, as other calcium phosphates may exhibit similar morphologies. For example, plate-like shapes are also characteristic for monetite ($CaHPO_4$) and brushite ($CaHPO_4{\cdot}2H_2O$), while octacalcium phosphate ($Ca_8(PO_4)_6(HPO_4)_2{\cdot}5H_2O$) has a petal-like character (Drouet, 2013). This makes it difficult to distinguish between these phases based on morphology alone.

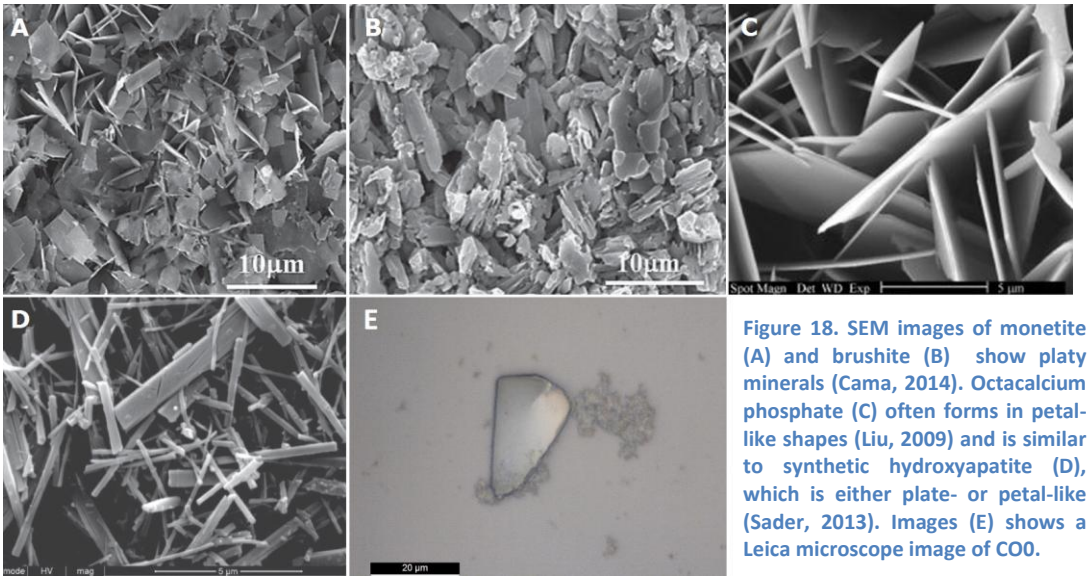


**Figure 18. SEM images of monetite (A) and brushite (B) show platy minerals (Cama, 2014). Octacalcium phosphate (C) often forms in petal-like shapes (Liu, 2009) and is similar to synthetic hydroxyapatite (D), which is either plate- or petal-like (Sader, 2013). Images (E) shows a Leica microscope image of CO0.**

The spectroscopic data provides important information that can be used to correctly identify what minerals are present in sample CO0. Figure 19 displays the FTIR data from sample CO0 (left) and spectra from various calcium phosphates (right). One easy way to tell apart hydroxyapatite and octacalcium phosphate from monetite and brushite is by looking at the presence of a peak around 962 $cm^{-1}$ (Drouet, 2013). This band represents the $v_1PO_4$ mode and is not visible in the spectra for brushite and monetite. As sample CO0 does display this band, the presence of monetite and brushite can be ruled out. Next, the spectral features of hydroxyapatite and octacalcium phosphate only have a few important differences. One of them is the presence of two distinct bands at 1195 and 916 $cm^{-1}$ in the octacalcium phosphate IR spectrum. They represent $HPO_4^{2-}$ ions in the crystal lattice and are not detectable for hydroxyapatite (Drouet, 2013). Similar bands to the ones that are mentioned are observed at 1209 and 914 $cm^{-1}$ in the spectrum for sample CO0. Along with the additional peak at 874 $cm^{-1}$, which is also related to $HPO_4$, this provides enough evidence to conclude that the FTIR data for sample CO0 shows significant indication that the mineral phase that was precipitated during synthesis of this particular sample, consists of octacalcium phosphate rather than hydroxyapatite.

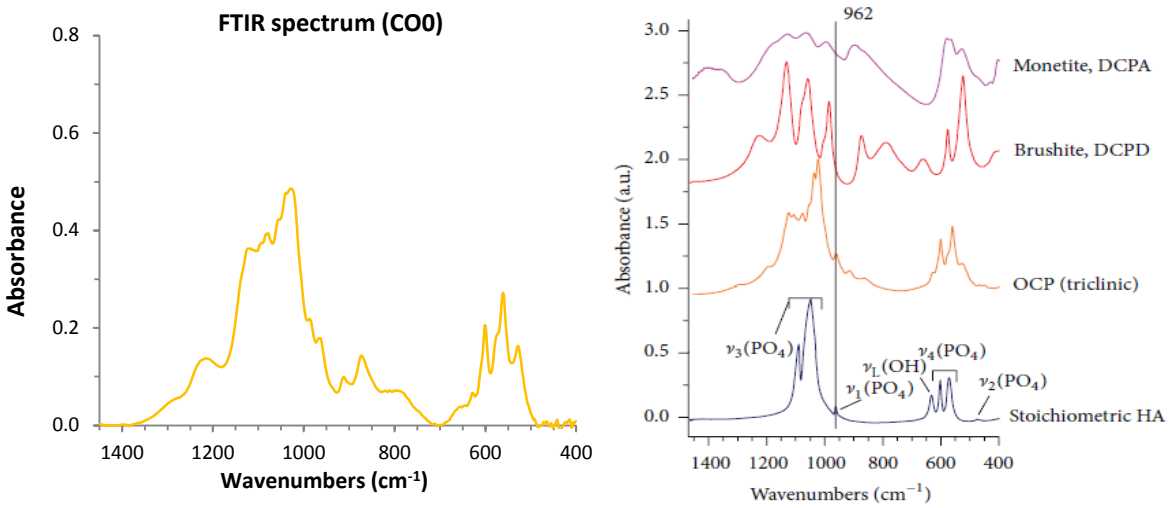


**Figure 19a (left): FTIR spectrum from sample CO0. Figure 19b (right): FTIR spectra from various calcium phosphates (Adapted from Drouet, 2013).**

Several hypotheses are suggested to explain the formation of octacalcium phosphate (OCP) instead of hydroxyapatite (HA). One of them is that OCP acted as a precursor phase to HA and that the experiment was ended before HA could be formed. Precursor phases are metastable minerals with a fast formation rate. This allows them to precipitate first, only to subsequently mature in solution over time (Tang, 2004). OCP consists of apatitic layers alternated with hydrated layers. It is a well-known precursor phase to the slow-forming HA, as it is similar in structure (Pompe, 2015).

The method used in this study to synthesise the samples was adapted from De Groot (2017), who aimed to monitor crystallinity and maturity changes over time. The initial calcium and carbonate-phosphate solutions were identical to the ones used in the current study. The only difference in methodology was that De Groot (2017) synthesised the samples at room temperature, while this study wanted to mimic the physiological conditions more closely, and performed the synthesis at 37 °C. Also, De Groot (2017) sampled the solution at regular intervals for 240 hours, while this study sampled the entire solution after 96 hours. The spectroscopic results from De Groot (2017) showed no signs of OCP in the carbonated samples, while the sample without added carbonate contained OCP during the entire synthesis experiment. De Groot (2017) concludes that OCP must have acted as a precursor phase in all samples and that carbonate most likely promoted hydrolysis of OCP into HA, causing the OCP to hydrolyse before it could be sampled and analyzed.

While the observations on OCP formation reported by De Groot (2017) are in agreement with results from the current study, De Groot's explanation is contradicted by Christoffersen (1989), who performed a similar experiment at a higher temperature (42°C) and initial pH 7.4. Results from Christoffersen (1989) indicated that OCP precipitated within the first 4 minutes of the experiment. A deficient form of hydroxyapatite (d-HA) was present after 44 minutes, and after 20 hours this form of apatite was the dominant phase. Therefore, the study by Christoffersen (1989) demonstrates the formation of hydroxyapatite within 20 hours in a synthesis solution without carbonate, while both the results from De Groot (2017) and the current study do not show any indication of the presence of apatite, even after much longer synthesis times. This suggests that another factor might be responsible for the preferred precipitation of octacalcium phosphate instead of hydroxyapatite.

An alternative explanation for the OCP formation is that the experimental conditions were simply not suitable for the formation of hydroxyapatite. It is well-known that temperature conditions affect the formation of certain mineral phases (Kumar, 2004), but in this experimental set-up, all samples were synthesised at identical temperatures. Therefore, this parameter could not have caused any (mineralogical) differences between the samples. Another factor that could have played a role is the pH of the solution during synthesis. As reported by Van Kemenade (1987), hydroxyapatite is the most stable calcium phosphate at pH 7.4 and above. Mineral phases such as OCP and monetite are more stable in acidic conditions and are therefore more likely to form (Elliott, 1994; Pompe, 2015).

Although the pH was not measured during the entire sample synthesis, the pH measurements during the first 60 minutes of the experiment provide a lot of useful information. As mentioned by Drouet (2013), the incorporation of OH- ions into the crystal structure during precipitation of hydroxyapatite can cause a decrease in solution pH. Visual observations indicate that most of the precipitation happens immediately after adding the carbonate-phosphate solution to the calcium chloride solution. Therefore, any changes in pH due to the uptake of $OH^-$ by the precipitate should occur shortly after mixing. This is confirmed by our pH data (Figure 5), which shows a significant drop in solution pH during the first 5 minutes of the synthesis of sample CO0. These findings confirm that the pH during synthesis of this sample was significantly lower than the level at which hydroxyapatite is likely to form (7.4), and simultaneously explains the formation of octacalcium phosphate, which is more stable at acidic conditions (pH 4-6.5; Pompe, 2015).

### Apatite formation in the presence of carbonate

Figure 20 compares the spectroscopic results from this study to the data from Sader (2013), who provides FTIR spectra for apatite samples with constant magnesium/calcium ratios and a varying carbonate content. The characteristic $v_3CO_3$ and $v_2CO_3$ bands that appear with increasing $CO_3^{2-}$ content in Figure 20c are clearly visible in Figure 20a and Figure 20b as well, confirming the presence of carbonate in samples CO1 to CO4. The fact that these $CO_3^{2-}$-related peaks are not equal in height indicates that the amount of carbonate varies for each sample. This is not surprising, as previous research found a positive correlation between the amount of carbonate added during synthesis and the resulting carbonate content (De Groot, 2017). However, this trend is not entirely in agreement with the results on incorporated carbonate in the current study (Figure 10a). While the $CO_3^{2-}$ content increases for CO0-CO3, sample CO4 does not follow the same trend and contains significantly less carbonate than expected. This indicates that not all the carbonate that was added during synthesis was incorporated into the minerals. As the samples in the current study were synthesised at 37°C and De Groot (2017) performed the synthesis experiment at room temperature, one possibility could be that the variation in results was caused by this temperature difference.

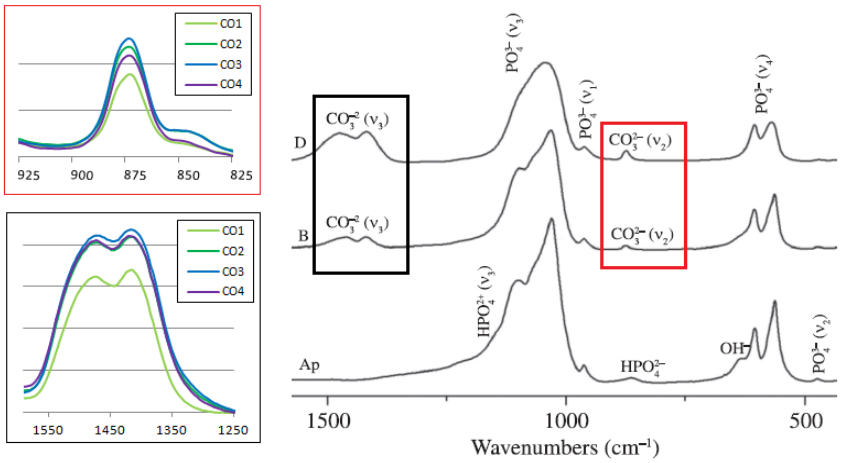


**Figure 20a (upper left): FTIR data of $v_2CO_3$ band. Figure 20b (lower left): FTIR data of $v_3CO_3$ band. Figure 20c (right): FTIR data of samples with similar Mg/Ca molar ratio and different $CO_3^{2-}$ content: hydroxyapatite (Ap), 3Mg/1C/1P (B) and 3Mg/5C/1P (D). Adapted from Sader (2013).**

Another factor that could have affected the trend in $CO_3^{2-}$ incorporation is that the apatite structure of sample CO4 was simply unable to take up more carbonate. If this was the case, a change in crystal habit could have occurred when high amounts of $CO_3^{2-}$ were added and the mineral was about to reach its maximum carbonate content. Several studies have observed morphological changes with increasing carbonate content. Most are dependent on the way carbonate is incorporated into the crystal structure. B-type carbonate is reported to cause shortening of the a-axis and lengthening in the c-axis due to the replacement of a big phosphate tetrahedron by a small planar carbonate ion (LeGeros, 1964; LeGeros, 1965). This ratio change between the a- and c-axes can result in the crystal shape evolution from large needle-like crystals to smaller rods, as observed in Sader (2013). On the other hand, A-type carbonate causes expansion of the a-axis and contraction in the c-axis when two hydroxyl groups are replaced by one carbonate ion (Elliott, 1964). While such morphological changes are reported abundantly, results from different studies show considerable variations. For example, Chickerur (1980) found that an increase in carbonate content caused a decrease of the a-axis that was much larger than reported by LeGeros (1964). Also, the c-axis did not change significantly when it was expected to increase. These deviations are attributed to differences in experimental conditions that either increase or decrease the likeliness of reprecipitation during formation of the solid phase (Chickerur, 1980). Furthermore, if the morphological change was caused by the abundant availability of carbonate, it is expected that the newly formed structure would be able to incorporate more $CO_3^{2-}$ and not less, as was observed in sample CO4.

While it is important to keep these studies in mind for further discussion, they do not explain if there is a maximum amount of carbonate that can be incorporated in the apatite structure and if so, how this could affect the mineral morphology. Also, while the Leica images (Figure 6) seem to indicate a slight change in morphology from sample CO1 to CO4, the high magnification AFM images (Figure 7) oppose this theory. They show that the big particles observed with the Leica microscope are in fact aggregates of small, kite-like minerals. The observation of decreasing crystal size with increasing carbonate content (Rodríguez-Lorenzo, 2000; Sader, 2013; Elliott, 1964), cannot be confirmed by our data. There are noticeable differences between the particles synthesised at different initial carbonate concentrations, but these changes do not particularly include the crystal shape or size. Instead, the changes occur primarily on the mineral surface, which becomes more irregular with increasing carbonate concentration during synthesis. Meanwhile, the characteristic kite-shaped particles can still be distinguished in each sample. This indicates that the crystal habit was not changed by the addition of high amounts of $CO_3^{2-}$, nor does it explain the relatively low carbonate content of sample CO4. Also, the fact that the irregularity of the crystals increased with initial carbonate concentration of the synthesis solution, instead of the amount of incorporated carbonate, suggests that the changing mineral surface wasn't solely caused by the amount of carbonate that was incorporated into the sample's crystal structure.

As there is not enough evidence to conclude that the addition of carbonate during sample synthesis caused a change in morphology of the precipitated minerals, it is likely that the irregular trend in carbonate incorporation is related to the initial synthesis conditions. The only chemical difference between the synthesis solutions was their carbonate concentration. However, something that cannot be overlooked is the effect of carbonate on the pH of a solution. As shown in Equation 1, the addition of carbonate results in an increase of the pH, as carbonate ions react with water to form bicarbonate and subsequently release hydroxide into the solution (Lower, 1999). This positive correlation is in agreement with Figure 21a, which plots the initial carbonate concentration against the solution pH after 60 minutes of synthesis. Furthermore, the pH values are relatively stable for the carbonated samples, while there was a big drop in pH for sample CO0 (Figure 5). This can be explained by the fact that Equation 1 is reversible and therefore reacts to the chemical environment by either producing or taking up $OH^-$. This buffering effect of carbonate will stabilise the pH (Lower, 1999).

Equation 1: $$CO_3^{2-} + H_2O \leftrightarrow HCO_3^- + OH^-$$

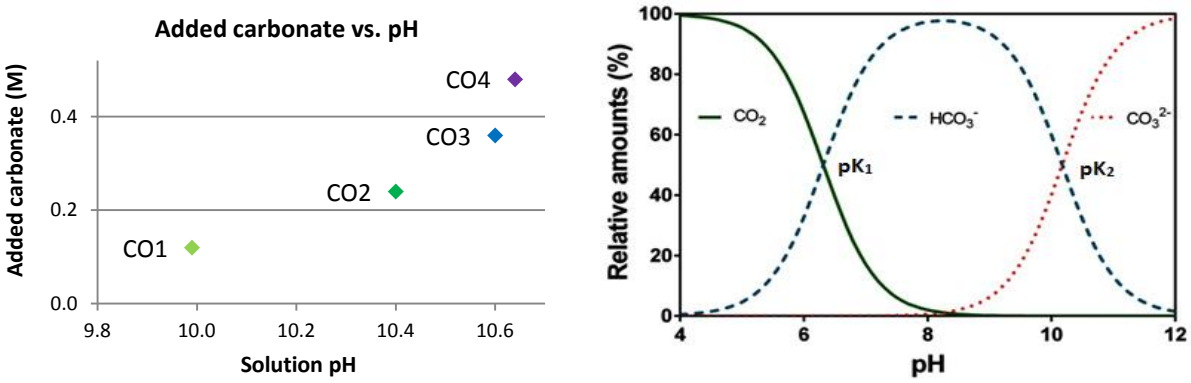


Figure 21a (left): Initial carbonate concentration of the carbonate phosphate solution (M) versus pH after 60 minutes of sample synthesis. Figure 21b (right): Relative speciation of $CO_2$, $HCO_3^-$ and $CO_3^{2-}$ as a function of pH. From Lower, 1999.

The importance of pH during (carbonate) hydroxyapatite precipitation is mentioned in several previous studies. Chickerur (1980) studied the hydrolysis of octacalcium phosphate into hydroxyapatite in solutions with different carbonate concentrations. They found a positive correlation between carbonate concentration and solution pH, which is in agreement with the data in Figure 5. Chickerur (1980) also reported that hydrolysis was incomplete for the solutions with high pH (>10.85), which resulted in a decrease in incorporated carbonate content. No further explanations were provided for this observation, other than that carbonate inhibited the hydrolysis process. Othman (2016) observed an increase in carbonate content of apatite samples that were synthesised at pH 8, 9 and 10, while a slight decrease in carbonate was witnessed in the sample with pH 11.

Finally, Yusufoglu (2008) studied carbonate incorporation under various pH conditions and reported an increase in $CO_3^{2-}$ content around pH 10 (Figure 22b). They also observed a morphological change from platy minerals at low pH (6.2) to prismatic hexagonal particles at higher pH (~10). These results fit the crystal habit of the carbonated sample particles as observed with the AFM and Leica microscope and the pH at which they formed. The trend of increasing carbonate incorporation around a specific pH as described by Yusufoglu (2008) is in agreement with the $CO_3^{2-}$ content in Figure 22a and could be related to the speciation of carbonate. According to Lower (1999), dissolved carbon is distributed among three species as a function of pH: $CO_2$, $HCO_3^-$ and $CO_3^{2-}$. The relative abundance of these species is shown in Figure 21b, where $pK_1$ and $pK_2$ are located around a pH of 6.35 and 10.33 in water with a temperature of 25 °C (Lower, 1999). When the pH value exceeds the $pK_2$, the speciation shifts from $HCO_3^-$ to $CO_3^{2-}$ abundance. In the current study, this could have had a negative effect on the incorporation of carbonate into the apatite lattice.

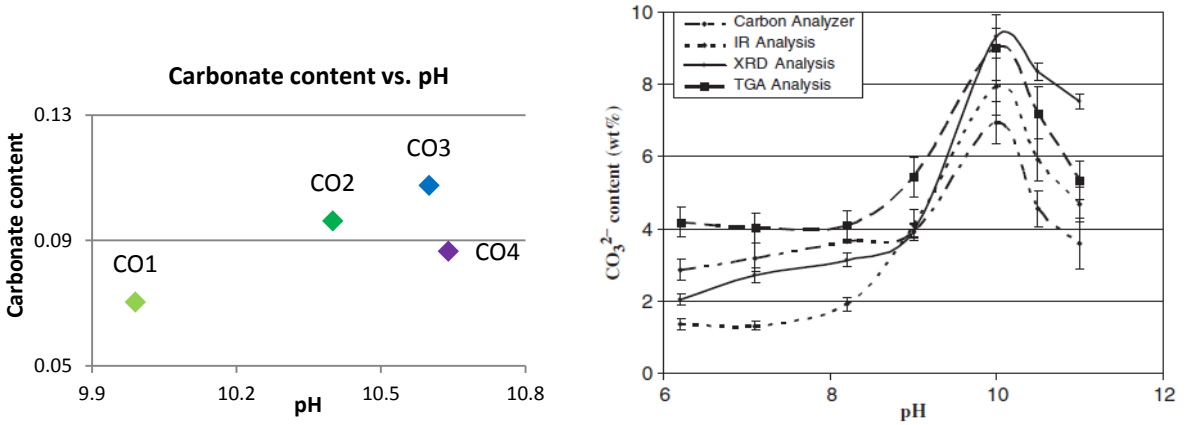


Figure 22a (left): Carbonate content determined from FTIR data versus the solution pH after 60 minutes of sample synthesis. Figure 22b (right): Relationship between $CO_3^{2-}$ content and solution pH as determined by a carbon analyzer, X-ray diffraction (XRD), infrared (IR), and thermal gravimetric analysis (TGA). From Yusufoglu, 2008.

However, Yusufoglu (2008) mentions maximum $CO_3^{2-}$ incorporation around a pH of 10, while this value lies around 10.5 in our data. This deviation could be explained by the difference in temperature when measuring the pH. Yusufoglu (2008) measured the pH at 20 °C, while samples CO0 to CO4 were analysed at 37 °C. The effect of temperature on pH measurements is reported by Barron (2006), who describes that a rise in temperature is associated with increased molecular vibrations, a decreased tendency to form hydrogen bonds and a subsequent increase of $H^+$ concentration. In water, this causes the measured pH to be roughly 0.32 units lower when measured at 40 °C compared to 20 °C (Clark, 2017). Also, the accuracy of the pH measurements during this experiment was not optimal, as the pH meter was calibrated at 20 °C.

Although it is likely that the observed trend in carbonate content is related to the variation in pH of the synthesis solutions, it doesn't directly explain the differences in carbonate substitution (Figure 10b). Given the shift in carbonate speciation around a pH of 10.33, it is possible that different types of substitution are preferred when different species are more abundant, but not much information can be found on this topic. The study by Madupalli (2017) does report that A-type substitution was only produced at significantly higher temperature than B-type carbonate, which indicates a higher energy barrier for the formation of A-type carbonate. This also explains why B-type carbonate is dominant in biological apatite, which is formed at a relatively low temperature.

As for the crystallinity of the samples, the negative correlation between crystallinity and carbonate concentration of the synthesis solution (Figure 12) can also be recognized when looking at the AFM and Leica images. Sample CO0 has a significantly higher crystallinity index than the other samples, which fits with the well-developed mineral surfaces. The carbonated samples display a different crystal habit, where the mineral surfaces become more irregular with increasing carbonate concentration during synthesis. Several studies have reported a decrease in crystallinity with increasing carbonate content (Sader, 2013; De Groot, 2017). This is often attributed to the fact that carbonate doesn't fit perfectly into the apatite lattice and therefore, more incorporated $CO_3^{2-}$ will result in a higher number of structural defects. However, in this study the crystallinity decreases with initial carbonate concentration instead of incorporated carbonate, suggesting that the actual carbonate content is not the only controlling factor. As reported by several studies, the way in which carbonate is incorporated also plays an important role in the mineral crystallinity. Madupalli (2017) studied structural changes in bone minerals in relation to carbonate substitution and found a strong correlation between the increase of A-type carbonate and a decrease in crystallinity index. Furthermore, Rey (1989) reported an increase in crystallinity as the amount of labile carbonate decreased during apatite maturation. This negative correlation is in agreement with the data in Figure 23, which shows a decrease in crystallinity as more labile and A-type carbonate are present. The increasing roughness of the sample surface can be attributed to the increase in labile carbonate, as this type of carbonate is thought to reside in the less crystalline, external apatite layers.

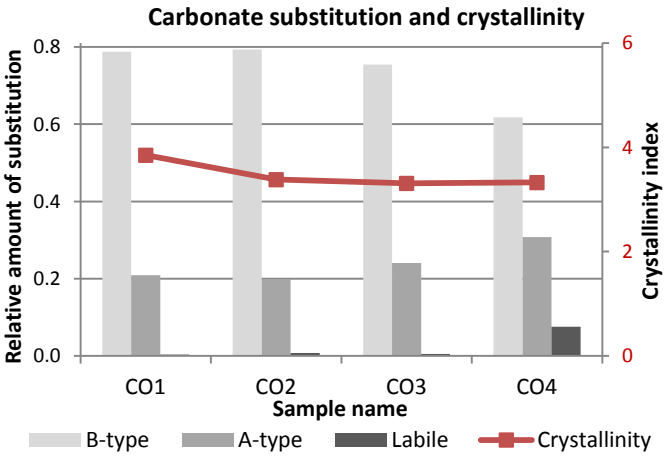


**Figure 23. The relative amount of carbonate substitution types for each sample is depicted by the three different bars, representing B-type, A-type and labile carbonate, respectively. The crystallinity index for each sample is displayed by the red line.**

## VII.II Solubility

### Phosphate content

As was mentioned previously, the AFM dissolution experiment proved to be more challenging than expected and did not result in any usable data. Therefore, only the data obtained from the bulk dissolution experiment will be discussed here. The dissolution was measured by exposing the sample powders to a buffered solution and monitoring the release of phosphate, which is a good way to evaluate the dissolution behaviour of apatite (Sader, 2013). The relatively stable phosphate concentrations during the final part of the experiment (60-150 minutes) indicate that dissolution had almost reached a maximum. The small value changes can be attributed to the experimental error margin during phosphate measurements. To test the total amount of phosphate in the samples, some sample powder was dissolved in hydrochloric acid. However, this experiment was repeated several times and resulted in significantly different values and trends each time. Therefore, it was decided not to use these results, but to assume that maximum phosphate release occurred after 150 minutes of dissolution. The observation that sample CO0 reaches considerably higher phosphate concentrations than the other samples (Figure 15) can be explained by the difference in chemical composition. Sample CO0 contains octacalcium phosphate, which is higher in phosphate than carbonated apatite. This can be deduced from the chemical formulas (Pompe, 2015):

$$Octacalcium\ phosphate:\ Ca_8H_2(PO_4)_6 \cdot 5H_2O$$

$$Carbonate\ hydroxyapatite:\ Ca_{10}(PO_4, CO_3)_6(OH)_2$$

According to Chickerur (1980), more carbonate incorporation into the apatite structure should result in lower phosphate concentrations. This trend is confirmed by the lines in Figure 15, which show a negative correlation between the amount of phosphate that is released after 150 minutes of dissolution and the carbonate content of the samples. The theory proposed by Chickerur (1980) relies on the carbonate being incorporated by B-type substitution, while labile and A-type carbonate are also observed in the current study (Figure 10b). The increase in these other types of substitution and the subsequent decrease in B-type carbonate can result in relatively higher phosphate levels, as fewer phosphate ions are replaced by carbonate, but this isn't observed in our data. Instead, the current study found that the amount of phosphate released from the carbonated samples at the end of the experiment is the biggest for sample C01, while CO3 has the lowest phosphate concentration. This fits with the trend expected by Chickerur (1980) and the large amounts of B-type substitution.

### Sample dissolution

Several studies report that carbonated apatite has a higher solubility than pure hydroxyapatite. This can be attributed to several factors. First of all, Sader (2013) reports that the bonds between calcium and phosphate are stronger than the bonds between calcium and carbonate, making carbonated apatite more susceptible to dissolution. Another important factor is that the solubility of a mineral increases when there are structural defects in the crystal structure (Baig, 1996), as this has a destabilizing effect on the mineral. Pure hydroxyapatite has fewer defects and a lower tendency to dissolve than carbonated apatite, as more structural defects occur with an increase in carbonate incorporation (Barry, 2002). Furthermore, B-type substitution causes a disruption of the charge balance, as $PO_4^{3-}$ ions are replaced by $CO_3^{2-}$. This can create vacant cation sites or result in coupled substitution, where carbonate is incorporated along with lower valence cations, to make up for the charge difference (Chickerur, 1980).

Due to the difficulty in analysing mineral structure and chemistry, these factors were not studied in detail during this study. Thus, it is not possible to say how the incorporation of carbonate in samples CO1-CO4 affected the type and location of other (cat)ions. Also, experimental conditions facilitated the precipitation of OCP rather than apatite in sample CO0. Comparing the solubility of these two different mineral phases would be unfitting when discussing the effect of carbonate on the dissolution of hydroxyapatite. However, this study did previously conclude that the crystallinity of the samples decreases when more carbonate is initially added to the synthesis solution. This is partly due to the increase in structural defects when more carbonate is incorporated into the apatite structure, but can also be attributed to the relative increase in labile and A-type carbonate at higher synthesis pH. As the crystallinity describes the lattice perfection and therefore its stability, minerals with a relatively low crystallinity should have a higher solubility. Contradictory to this hypothesis, the data in Table 6 shows that the initial dissolution of sample CO3 is significantly more rapid than that of CO2 and CO4, even though their crystallinity indexes are almost equal (Figure 12). This suggests that factors other than crystallinity control the mineral solubility and dissolution rates.

LeGeros and Tung (1983) synthesised different carbonated apatites and exposed them to an acid buffer while the dissolution was measured in mMol calcium per mL buffer solution. They found that the extent of dissolution was proportional to the carbonate content of the apatite, which is in agreement with the high $CO_3^{2-}$ content and quick initial dissolution of sample CO3 in the current study. Other studies report that minerals with a high carbonate content are especially susceptible to dissolution in acidic conditions, which could be related to the speciation of carbonate. As Figure 21b shows, $CO_3^{2-}$ is converted to $CO_2$ when the solution pH is below the $pK_1$ value (6.35 at 25 °C). This could promote the dissolution process and explain why the dissolution test using a solvent with pH 4.5 resulted in the immediate dissolution of the CO3 sample material (Figure 13a).

Samples CO1, CO2, and CO4 display significantly lower initial dissolution rates than CO3, but do follow the trend of quicker dissolution with increasing carbonate content. This can be seen in Figure 24, which displays the positive correlation between $CO_3^{2-}$ content and the phosphate release during the first 10 minutes of dissolution. As mentioned before, octacalcium phosphate is most stable at pH 4-6.4 (Pompe, 2015). This explains the rapid dissolution of sample CO0, as a solution with pH 6.5 was used. Another factor that could increase the solubility of OCP, is the fact that platy minerals such as the ones observed in this sample have a high surface area, which increases the amount of sample that is in contact with the surrounding solution and the surface on which dissolution can take place.

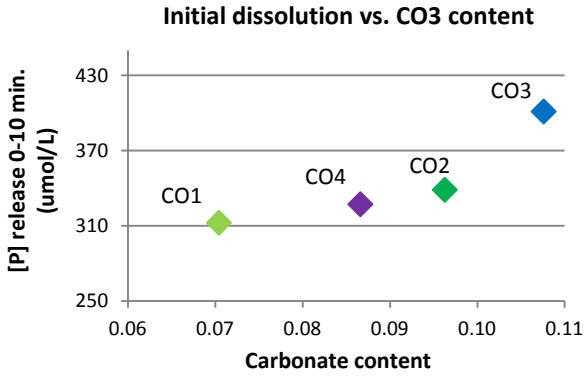


**Figure 24. Initial dissolution rates in µMol/L for the first 10 minutes of the bulk dissolution experiment, versus the carbonate content of the samples.**

## Changes in morphology and composition

The extra samples that were taken after 60 minutes of dissolution were dried on a silicon wafer and imaged by AFM analysis, to see if any morphological changes had occurred in the dissolving minerals. The results show that the remaining particles are very rounded, as opposed to the minerals prior to dissolution, which had a clearly defined shape. This could indicate that the dissolution was most effective at the mineral corners, resulting in the removal of material mostly at these locations. Raman spectroscopic analysis was conducted to provide more information on the mineralogy of the remaining particles. Most of them seemed to be highly hydrated, as they disintegrated within seconds after the Raman laser was turned on, even when it was on a very low intensity. Also, the signal from the silicon wafer surface was so strong that it often obscured the signal of the mineral particles. Despite these problems, a few good spectra were obtained. Peak characterisation indicated that most of the bands were formed by vibrations of phosphate and organic molecules.

The presence of the CH bands and Amide I and III peaks is most likely due to the MES buffer ($C_6H_{13}NO_4S$) in the solvent. As the samples were prepared by dropping the solution onto a silicon wafer and evaporating the aqueous phase, it is possible that some residue of the buffer was left behind on the surface, along with the mineral particles. However, the organic-related peaks were only observed when scanning the particles, not when obtaining a spectrum was of the wafer surface. Given the strong signal of the silicon, it could be possible that organics were present on the surface, but that their vibrational bands were obscured by the silicon peaks. This doesn't seem likely, as the organic-related bands were primarily observed in samples with a relatively high carbonate content (CO2-CO4). This suggests that the organics were only present in or on the particles and that this interaction might have been promoted by the carbonate content of the samples.

With the exception of the $v_1PO_4$ peak at 961 $cm^{-1}$, the phosphate bands of the dissolved particles are relatively weak. Close-ups of the 900-1100 $cm^{-1}$ region of the Raman data from both before and after dissolution are shown in Figure 25. Comparing the two graph shows that the $HPO_4$ molecules have disappeared from sample CO0 during dissolution and that an additional $v_3PO_4$ band has appeared in all samples. Also, the amount of carbonate decreased significantly for CO1-CO4, but sample CO4 experienced the highest loss of $CO_3^{2-}$. This might be related to the relatively large amount of labile carbonate in this sample, which is less stable than the other carbonate types and therefore more soluble. Furthermore, the phosphate peaks of the dissolved particles vary considerably in height and shape throughout the spectra, which makes it difficult to estimate the relative amounts of phosphate for each sample. However, it can be concluded that $PO_4^{3-}$ is present in considerable amounts.

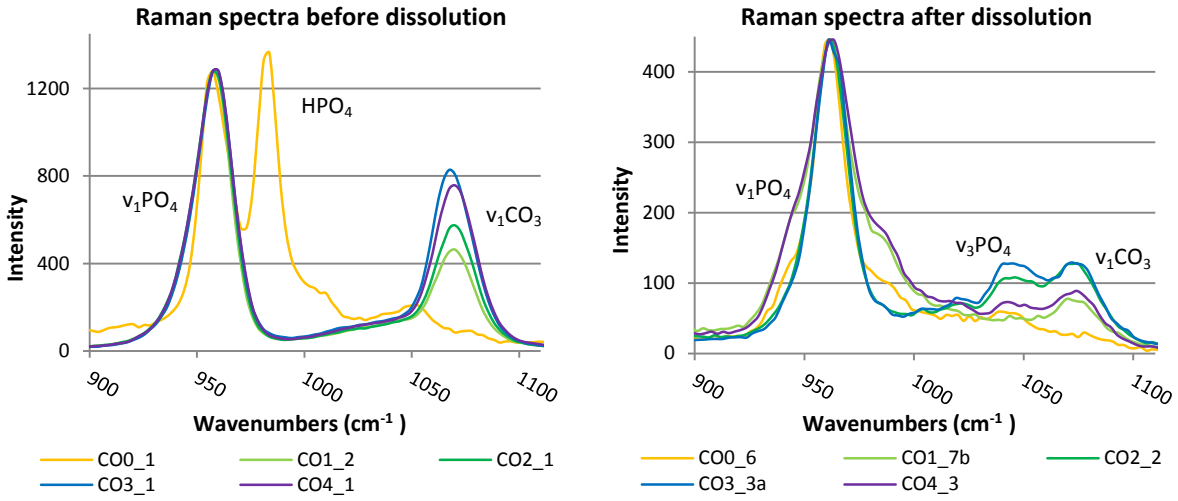


Figure 25. Raman spectra of the samples before dissolution (left) and after 60 minutes of dissolution (right).

The presence of phosphate here is somewhat surprising, considering that the particles had already been dissolving for 60 minutes and that phosphate release had almost reached a steady state by that time. Visual observations also confirm that a significant amount of solid particles is still present after 90 minutes of dissolution. There are several theories on why so many phosphate-rich particles are left, even when the phosphate release has reached a steady state. Boudia (2018) studied hydroxyapatite dissolution by monitoring the changes in solution composition and mineral surface. Spectroscopic results indicated the formation of a new, solid phase during dissolution and FTIR analysis concluded that this phase consisted of monetite ($CaHPO_4$). As the solutions were not saturated with respect to any secondary phase, a classical precipitation process by oversaturation was excluded. Instead, Boudia (2018) proposed that stoichiometric Ca/P release was followed by an interfacial dissolution-precipitation reaction, which resulted in the formation of the new phosphate phase. According to Boudia (2018), monetite starts to precipitate around 8 hours after the start of the dissolution experiment, when the Ca/P ratio of the solution starts to decrease. Considering that the dissolution time of our samples is much shorter, it is unlikely that the particles observed in Figure 16 consist of monetite. This is confirmed by the Raman data of monetite presented in Casciani (1980), which doesn't match the results of the current study. However, the findings by Boudia (2018) do suggest that a new phase such as monetite might have formed if the experiment had lasted for a longer time. Also, it is possible that mineralogical changes were already occurring during the initial stage of the experiment.

Tang (2004) provides a different hypothesis by suggesting that mineral dissolution may be inhibited or even suppressed when the size of the dissolving particle falls within a certain range. The study reports that synthetic hydroxyapatite minerals became continuously smaller during dissolution, until they were at the nano-scale size and did not dissolve any further, despite being in undersaturated solutions (Tang, 2004). Spectroscopic IR results showed that the residual particles were similar in composition to the ones prior to dissolution, which is contradictory to the results by Boudia (2018), but in agreement with the results of the current study. Tang (2004) suggests that the nano-scale particles were kinetically protected against further dissolution, as the mineral surfaces became too small for dissolution pits to form. Studies report that only pits larger than a certain size will actively contribute to the dissolution of a mineral, so when the crystal surfaces are near this critical size, dissolution rate will decrease or even stop completely. The critical surface area size is dependent on the type of mineral that is dissolving and is estimated to be around 50 nm for dental enamel and roughly 200-500 nm for synthetic apatite (Tang, 2004). The residual particles detected in the current research vary in size but are mostly between 300 and 600 nm. This suggests that the theory explained in Tang (2004) could be responsible for the apparent steady state of phosphate, as the residual particles are simply becoming too small for dissolution pits to be significant.

Finally, the possible effects of the MES buffer in the solvent cannot be overlooked. Although Raman spectroscopy confirms the presence of organic-related peaks when analysing the dissolved particles, it is difficult to say if these molecules form a layer of residue over the entire sample, or that they are actually incorporated into the mineral structure. As the incorporation of new molecules changes the mineral chemistry, the chemical stability is also affected. Therefore, the presence of organics in the mineral structure could have caused either a higher or lower dissolution rate. However, there is not enough information to say if and how the presence of the MES buffer has affected the particles during dissolution, but it would be an interesting topic for further research.

# VIII. CONCLUSIONS

The aim of this study was to see how the solubility of synthetic hydroxyapatite minerals was affected by their carbonate content. Five different samples were synthesised in such a way that the only variable was the amount of carbonate added during synthesis. The resulting precipitates were analyzed by Fourier transform infrared spectroscopy and Raman spectroscopy to determine the crystallinity, carbonate content and types of carbonate substitution. Atomic force microscopy (AFM) and the Leica microscope were used to obtain images of the sample particles before dissolution. The AFM was also used to monitor changes on the mineral surface during an *in situ* dissolution experiment, but this did not result in usable data. Furthermore, a specific amount of sample powder was dissolved in a buffered solution with pH 6.5. During this bulk dissolution experiment, samples were extracted from the solutions at regular time intervals. Next, the phosphate concentration of these samples was measured using the molybdenum blue colourimetric method. Extra samples were taken after 60 minutes of bulk dissolution and analysed by the AFM and Raman spectroscopy.

The results of this study show considerable differences between both the morphology and chemistry of sample CO0 and CO1-CO4. The precipitated minerals in CO0 (Figure 6a) were expected to consist of pure hydroxyapatite, but spectroscopic data revealed that the solid phase was octacalcium phosphate (OCP). The lack of apatite formation during synthesis of this sample was attributed to the solution pH, as apatite is most likely to form at pH > 7.4, while the pH during synthesis was around 5.2 (Figure 5). Octacalcium phosphate is more stable at acidic conditions where the pH is between 4 and 6.4, which explains its precipitation during synthesis of sample CO0. It also explains why the OCP minerals experienced very high dissolution rates when being exposed to a solution with pH 6.5. Furthermore, the platy octacalcium phosphate minerals have a relatively big surface area on which dissolution pits can grow. This actively contributes to the dissolution of the mineral.

The presence of carbonate in samples CO1-CO4 is confirmed by the characteristic $v_3CO_3$ and $v_2CO_3$ bands that appear in the spectra (Table 4 and Table 5). These carbonated samples display similar crystal habits that resemble triangular, pentagonal, and hexagonal shapes. Observing the particles at a higher magnification reveals that they consist of aggregates of multiple, subhedral minerals with a kite-like shape (Figure 7). While these shapes are present in all carbonated samples, the mineral surfaces are very smooth for sample CO1 and become increasingly rougher towards CO4. This can be attributed to the increase in labile carbonate (Figure 10b), which subsequently causes a decrease in crystallinity for the samples where more carbonate was initially added during the synthesis process (Figure 12). Some studies report a change in crystal size as more carbonate is incorporated into the structure. The substitution of a planar $CO_3^{2-}$ ion for the $PO_4^{3-}$ tetrahedron (B-type carbonate) causes contraction in the a-axis and expansion in the c-axis, while the replacement of one carbonate ion by two hydroxyl groups (A-type substitution) will cause expansion of the a-axis and contraction in the c-axis. However, such changes in mineral size were not observed in the current study.

The results for the carbonate content of the synthesised samples (Figure 10a) show that the amount of $CO_3^{2-}$ increases from sample CO0 to CO3 and drops for CO4. A positive correlation was found between initially added carbonate and the pH of the synthesis solution (Figure 22a). Also, several studies report that carbonate incorporation into the apatite lattice is most favourable around a specific synthesis pH. This can be attributed to the speciation of carbonate, as $CO_3^{2-}$ becomes more abundant than $HCO_3^-$ when the solution pH exceeds 10.33 (Figure 21b), which is likely to affect the incorporation of carbonate into the apatite structure. The value around which maximum carbonate content occurred was pH 10 in some studies, while it was 10.5 in the current research. However, this study performed the pH measurements at a higher temperature, which most likely resulted in slightly higher pH values. Therefore, it can be concluded that the carbonate content of the samples is related to the pH of their synthesis solution, which was increased when more carbonate was added. The positive correlation between labile and A-type carbonate and the amount of initial carbonate is also related to the increase of synthesis pH, which could also be attributed to carbonate speciation.

When substitution takes place within a mineral, the normal crystal structure is compromised. This often results in small structural defects that destabilise the mineral and increase its solubility. It is thought to be the main reason that carbonated apatite has a higher solubility than pure, stoichiometric hydroxyapatite. All the hydroxyapatite that precipitated during our experiments contained carbonate, so the dissolution rates cannot be compared to a pure hydroxyapatite sample, but the results did show a positive correlation between the carbonate content and dissolution rate (Figure 24). Sample CO3, which contains significantly more carbonate, also displays the highest initial dissolution rate (apart from CO0), while CO1 has a lower $CO_3^{2-}$ content and dissolves considerably slower. Results also show that the crystallinity of the precipitated minerals decreases as more carbonate was added to the synthesis solution. As the crystallinity describes the perfection of the crystal structure and decreases when more structural defects are present, it is likely that minerals with a lower crystallinity have higher dissolution rates. However, samples CO2, CO3, and CO4 have similar crystallinity indexes but very different dissolution rates. This suggests that crystallinity is not the only factor that controls the solubility, but that carbonate content also plays an important role.

Finally, the AFM and Raman analysis of the dissolved particles indicated that they consisted mostly of phosphate, carbonate, and some organic molecules such as Amide I and Amide III. Other bands may have been present, but it is likely that they were obscured by the intense signal of the silicon wafer on which the particles were precipitated. The organics were not observed prior to dissolution and are therefore introduced to the system by the MES buffer, which was added to the solution in which the particles were dissolved. As it is not clear if the components of the buffer were actually incorporated into the mineral structure, or that they were only present on the surface, it is difficult to say if and how the MES buffer interfered with the dissolution process. Furthermore, the considerable amount of phosphate in the dissolved particles is somewhat surprising, considering that the phosphate release was near steady state when these samples were taken. Several hypotheses are proposed to explain this observation. First, studies report the presence of a new solid phase after the occurrence of dissolution-reprecipitation, but this usually occurs after several days of dissolution. Plus, the Raman data confirmed that the particle chemistry was similar to before dissolution. A more convincing theory is that the particles were about to reach a critical size, where the mineral surfaces are too small for effective dissolution pits to form. This could have inhibited mineral dissolution and make it appear as though steady state had been reached.

Finally, it can be concluded that the solubility of hydroxyapatite minerals increases significantly when more carbonate is incorporated into the structure. This has important implications for people who suffer from bone-related diseases such as X-linked hypophosphatemia, where the body disposes of the phosphate ions that are released during bone remodelling, instead of reabsorbing them into the bloodstream. This results in a phosphate deficiency when forming new bone minerals and the preferential uptake of carbonate into the apatite structure. As was concluded in this study, there is a positive correlation between carbonate content and solubility. This higher solubility will furthermore results in a quicker bone remodelling process, as the minerals are easier to dissolve. This only contributes to the problem, as more phosphate will be released, increasing the amount of carbonate incorporation and thus, increasing the mineral solubility. For further research, it would be useful to look into the exact effect of pH on carbonate incorporation and substitution type, and to see if and how the changes that occurred in this study due to a variation in pH, compare to biological bone minerals. Also, it would be interesting to see if the incorporation of others ions alongside carbonate might have an effect on the mineral solubility.

# REFERENCES


- Adler CP. 2000. Bones and bone tissue; normal anatomy and histology. In: *Bone Diseases*. 1-30.

- Anderson RE, Woodbury DM, Webster SSJ. 1986. Humoral and Ionic Regulation of Osteoclast Acidity. *Calcif Tissue Int*. 39:252-258.

- Baig AA, Fox JL, Hsu J, Wang Z, Otsuka M, Higuchi WI, LeGeros, RZ. 1996. Effect of carbonate content and crystallinity on the metastable equilibrium solubility behavior of carbonated apatites. *Journal of colloid and interface science.* 179(2):608-617.

- Baron R. 1995. Molecular mechanisms of bone resorption: An Update. *Acta Orthopaedica Scandinavica*. 66(266):66-70.

- Baron R, Neff L, Louvard D, Courtoy P. 1985. Cell-mediated Extracellular Acidification and Bone Resorption: Evidence for a Low pH in Resorbing Lacunae and Localization of a 100-kD Lysosomal Membrane Protein at the Osteoclast Ruffled Border. Journal of Cell Biology. 101:2210-2222.

- Barron JJ, Ashton C, Geary L. 2006. The Effects of Temperature on pH Measurement. *57th Annual Meeting of the International Society of Electrochemistry.*

- Barrows JN, Jameson GB, and Pope MT. 1985. Structure of a heteropoly blue. The four electron reduced beta-12-molybdophosphate anion. *J. Am. Chem. Soc.* 107:1771.

- Barry AB, Baig AA, Miller SC, Higuchi WI. 2002. Effect of age on rat bone solubility and crystallinity. *Calcif Tissue Int*. 71(2):167-71.

- Bone Research Society. 2017. Osteoclast resorption #4. Retrieved from http://boneresearchsociety.org/resources/gallery/40/#top on 01-11-2017.

- Boudia S, Zuddas P, Fernane F, Fiallo M, Sharrock P. 2018. Mineralogical transformation during hydroxyapatite dissolution in simple aqueous solutions. Chemical Geology. 477:85–91.

- Carpenter, TO. 1997. New perspectives on the biology and treatment of S-linked hypophosphatemic rickets. *Pediatric endocrinology*. 44(2): 443-466.

- Casciana F, Condrate RA. 1980. The Raman Spectrum of Monetite, CaHP04. *Journal of Solid State Chemistry*. 34:385-388.

- Cazalbou S, Combes C, Eichert D, Rey C, Glimcher MJ. 2004. Poorly crystalline apatites: evolution and maturation in vitro and in vivo. *Journal of bone and mineral metabolism*. 22(4):310-317.

- Chambers TJ, Revell PA, Fuller K, Athanasou NA. 1984. Resorption of Bone by Isolated Rabbit Osteoclasts. *J. Cell Sci.* 66:383-399.

- Chickerur NS, Tung MS, Brown WE. 1980. A mechanism for incorporation of carbonate into apatite. *Calcified Tissue International*. *32*(1):55-62.

- Christoffersen J, Christoffersen MR, Kibalczyc W, Andersen FA. 1989. A contribution to the understanding of the formation of calcium phosphates. *Journal of Crystal Growth*. 94(3): 767-777.

- Clark, J. 2017. Temperature Dependence of the pH of pure water. Retrieved from https://chem.libretexts.org/Core/Physical_and_Theoretical_Chemistry/Acids_and_Bases/Acids_and_Bases_in_Aqueous_Solutions/The_pH_Scale/Temperature_Dependence_of_the_pH_of_pure_Water on 05-02-2018.

- Crane NJ, Popescu V, Morris MD, Steenhuis P, & Ignelzi MA. 2006. Raman spectroscopic evidence for octacalcium phosphate and other transient mineral species deposited during intramembranous mineralization. *Bone. 39*(3):434-442.

- Delgado-López JM, Iafisco M, Rodríguez I, Tampieri A, Prat M, Gómez-Morales J. 2012. Crystallization of bioinspired citrate-functionalized nanoapatite with tailored carbonate content. *Acta Biomaterialia*. 8:3491-3499.

- Drouet C. 2013. Apatite formation: why it may not work as planned, and how to conclusively identify apatite compounds. *BioMed research international*.

- Elliott, JC. 1964. The crystallographic structure of dental enamel and related apatites, Ph.D. Thesis, University of London.

- Elliott, JC. 1994. Structure and Chemistry of the Apatites and Other Calcium Orthophosphates. *Elsevier Science*.

- Fleet ME, Liu X. 2004. Location of type B carbonate ion in type A–B carbonate apatite synthesized at high pressure. *J Solid State Chem*. 177:3174-3182.

- Fleet ME, Liu X, King PL. 2009. Accommodation of the carbonate ion in apatite: An FTIR and X-ray structure study of crystals synthesized at 2–4 GPa. *American Mineralogist.* 89:1422-1432.

- De Groot, R. 2017. The influence of carbonate on the maturation process of poorly crystallized apatite under inorganic conditions and under the presence of the organic molecule citrate. *Guided research project at Utrecht University*.

- Hadjidakis DJ, Androulakis II. 2006. Bone remodelling. *Ann. N.Y. Acad. Sci.* 1092:385-396.

- International Osteoporosis Foundation 1. 2017. What is osteoporosis? Retrieved from https://www.iofbonehealth.org/what-is-osteoporosis on 20-08-2017.

- International Osteoporosis Foundation 2. 2017. Introduction to bone biology: all about our bones. From: https://www.iofbonehealth.org/introduction-bone-biology-all-about-our-bones. Retrieved on 20-08-2017.

- Ivanova TI, Frank-Kamenetskaya OV, Kol'tsov AB, Ugolkov VL. 2001. Crystal structure of calcium-deficient carbonated hydroxyapatite. Thermal decomposition. *J Solid State Chem*. 160:340-349.

- Khan AF, Awais M, Khan AS, Tabassum S, Chaudhry AA & Rehman IU. 2013. Raman Spectroscopy of Natural Bone and Synthetic Apatites. *Applied Spectroscopy Reviews*. 48(4):329-355.

- Van Kemenade MJJM, de Bruyn PL. 1987. A Kinetic Study of Precipitation from Supersaturated Calcium Phosphate Solutions. *J. Colloid Interface Sci.* 118: 564-585.

- Köhler S, Vasilevsky N, Engelstad M, Foster E. 2017. The Human Phenotype Ontology in 2017. *Nucl. Acids Res*.

- Kumar R, Prakash KH, Cheang P, Khor KA. 2004. Temperature Driven Morphological Changes of Chemically Precipitated Hydroxyapatite Nanoparticles. *Langmuir*. 20:5196-5200.

- LeGeros RZ. 1965. Effect of carbonate on the lattice parameters of apatite. *Nature*. 206:403.

- LeGeros RZ, LeGeros JP, Trautz OR, Klein E. 1964. Spectral properties of carbonate in carbonate containing apatites. *J. Dent. Res.* 43:751.

- LeGeros RZ and Tung MS. 1983. Chemical Stability of Carbonate- and Fluoride-Containing Apatites. *Caries Res*. 17:419-429.

- Leventouri, T. 2006. Synthetic and biological hydroxyapatites: Crystal structure questions. *Biomaterials*. 27:3339-3342.

- Liu Y, de Groot K, Hunziker EB. 2009. Biomimetic mineral coatings in dental and orthopaedic implantology. *Frontiers of Materials Science in China*. 3(2):154–162.

- Lower SK. 1999. Carbonate equilibria in natural waters. In: *Chem 1. Environmental Chemistry – Chapter 10.*

- Lu X. and Leng Y. 2005. Theoretical analysis of calcium phosphate precipitation in simulated body fluid. *Biomaterials*. 26(10): 1097-1108.

- Madupalli H, Pavan B, Tecklenburg MMJ. 2017. Carbonate substitution in the mineral component of bone: Discriminating the structural changes, simultaneously imposed by carbonate in A and B sites of apatite. *Journal of Solid State Chemistry.* 255:27-35.

- Marie PJ, Glorieux FH. 1981. Histomorphometric study of bone remodelling in hypophosphatemic vitamin D-resistant rickets. *Metab. Bone Dis. Rel. Res*. 3:31-39.

- National Center for Biotechnology Information. 2017. PubChem Compound Database. Obtained from https://pubchem.ncbi.nlm.nih.gov/ on 25-10-2017.

- Othman R, Mustafa Z, Wee Loon C, Noor, AFM. 2016. Effect of calcium precursors and pH on the precipitation of carbonated hydroxyapatite. *Procedia Chemistry*. 19:539-545.

- Pedersen O, Colmer TD, Sand-Jensen K. 2013. Underwater Photosynthesis of Submerged Plants - Recent Advances and Methods. *Frontiers in Plant Science*. 4:140.

- Penel G, Leroy G, & Bres E. 1998. New preparation method of bone samples for Raman microspectrometry. *Applied spectroscopy*. *52*(2):312-313.

- Pompe W, Worch H, Habraken WJEM, Simon P, Kniep R, Ehrlich H, Paufler P. 2015. Octacalcium phosphate – a metastable mineral phase controls the evolution of scaffold forming proteins. *J. Mater. Chem. B. 3:5318-5329.*

- Qin A, Cheng TS, Pavlos NJ, Lin Z, Dai KR, Zheng MH. 2012. V-ATPases in osteoclasts: Structure, function and potential inhibitors of bone resorption. *The International Journal of Biochemistry & Cell Biology.* 44:1422- 1435.

- Raggatt LJ, Partridge NC. 2010. Cellular and Molecular Mechanisms of Bone Remodelling. *J. Biol. Chem*. 285(33):25103-25108.

- Rehman I & Bonfield W. 1997. Characterization of hydroxyapatite and carbonated apatite by photo acoustic FTIR spectroscopy. *Journal of Materials Science: Materials in Medicine*. *8*(1):1-4.

- Ren F, Ding Y, Leng Y. 2014. Infrared spectroscopic characterization of carbonated apatite: A combined experimental and computational study. *J Biomed Mater Res Part A*. 2014:102A:496–505.

- Rey C, Collins B, Goehl T, Dickson IR, Glimcher MJ. 1989. The Carbonate Environment in Bone Mineral: A Resolution-Enhanced Fourier Transform Infrared Spectroscopy Study. Calcif Tissue Int. 45:157-164.

- Rodríguez-Lorenzo LM, Vallet-Regi M. 2000. Controlled Crystallization of Calcium Phosphate Apatites. *Chem. Mater.* 12:2460-2465.

- RRUFF, 2018. *Silicon R050145, Raman spectrum.* Obtained from http://rruff.info/Silicon on 13-02-2018.

- Sader MS, Lewis K, Soares GA, LeGeros RZ. 2013. Simultaneous Incorporation of Magnesium and Carbonate in Apatite: Effect on Physico-chemical Properties. *Materials Research*. 16(4):779-784.

- Sharkey MS, Grunseich K, Carpenter TO. 2015. Contemporary Medical and Surgical Management of X-linked Hypophosphatemic Rickets. *The American Academy of Orthopaedic Surgeons*.

- Skinner, HCW. 1989. Low temperature carbonate phosphate materials or the carbonate apatite problem: a review. *Origin, evolution and modern aspects of biomineralization in plants and animals*. 251-264.

- Tang R, Wang L, Orme A, Bonstein T, Bush PJ, Nancollas GH. 2004. Dissolution at the Nanoscale: Self-preservation of Biominerals. *Angew. Chem*. 116:2751-2755.

- Uchinokura K, Sekine T, Matsuura E. 1972. Raman Scattering by Silicon. *Solid State Communications*. 11:47-49.

- Väänänen HK, Karhukorpi EK, Sundquist K, Wallmark B, Roininen I, Hentunen T, Tuukkanen J, Lakkakorpi P. 1990. Evidence for the Presence of a Proton Pump of the Vacuolar H+-ATPase Type in the Ruffled Borders of Osteoclasts. *The Journal of Cell Biology.* 111:1305-1311.

- Väänänen, HK, Zhao, H, Mulari, M. 2000. The cell biology of osteoclast function. *J. Cell Sci.* 113(3): 377-381.

- Wallace, J. 2017. General Introduction to Bone: Collagen and Mineral. Retrieved from Bone Biology and Mechanics Lab at http://www.iupui.edu/~bbml/boneintro.html on 19-11-2017.

- Yusufoglu, Y and Akinc M. 2008. Effect of pH on the Carbonate Incorporation into the Hydroxyapatite Prepared by an Oxidative Decomposition of Calcium–EDTA Chelate. *J. Am. Ceram. Soc*. 91(1):77-82.

# Appendix A. Detailed methodology

### Sample synthesis

De Groot follows the recipe of Delgado-Lopéz (2012) to make two mixtures of a calcium solution and a carbonate-phosphate solution, one in which citrate is added to the calcium solution and one without citrate. For this experiment it was decided to synthesise the samples without adding citrate. Our main interest lies in what happens to the solubility when phosphate is replaced by carbonate, so preferably the synthesised samples are high in carbonate and low in phosphate. In theory, the presence of citrate promotes the uptake of phosphate in the samples. Also, previous research showed that samples containing citrate have a larger variation in carbonate content than non-citrate samples. Finally, adding citrate would possibly results in samples that are more similar to biological, bone-like apatite, but it would also increase the difficulty in their analysis and characterisation. Therefore, it was decided not to use citrate, but keep it in mind when thinking about further research suggestions.

Sampling of the solutions was done by mixing the solution on the stirring plate, turning the septum bottle upside down and quickly using a needle and syringe to extract the required amount of solution before separation of the precipitates and liquid could occur.

### FTIR analysis

The first way of obtaining a suitable sample powder, which was used for samples CO0 and CO1, was done by scooping out some of the frozen sample, placing it in the mortar and spraying it with ethanol. After this, the mixture was crushed using a mortar and pestle. The final mixture was poured onto a glass plate and left to dry. However, evaporation of the water went slower than expected due to the large amount of water. Therefore, it was decided to let the samples defrost and separate into a liquid and a solid part, and use a pipette to extract the solid particles from the bottom of the tube. The mixing and crushing was done in the same manner as before, and to allow the samples to dry completely, they were placed in the oven on 35 °C for about half an hour, until only a dry powder was left on the glass plate.

### AFM sample preparation

Two different ways were tried to obtain a thin layer of precipitates on the silicon wafer. For the first method the tube was mixed by placing it on the Vortex-Genie 2 for ten seconds. When the solution and precipitate were mixed properly, a pipette was used to extract about 20 µL from the tube and drop it onto the silicon wafer, which was placed on a glass plate. This process was repeated for each sample. However, after the samples were left to dry for about 15 minutes, it became clear that the silicon wafers were covered with a thick layer of (loose) precipitate, which isn't suitable for AFM analysis as this requires the particles to remain steady and flat during tip scanning. The second method is described in the main report and obtained better results. For this method, a smaller amount (5 µL) was placed onto the silicon wafer and it was sprayed with isopropanol (96%) until the solution was diluted enough to cover the surface with a fine layer of particles. By tapping the sides of the glass plate, the particles were distributed equally around the wafer surface.

After the first try of preparing the silicon wafers for the AFM experiment, the samples were subjected to a test-scan. The silicon wafers were stuck on a small metal plate and placed on the magnetic AFM sample holder. When trying to scan the surface of the bigger particles (100 µm), they did not remain stuck on the surface, but were moved around by the tip of the cantilever, making it impossible to obtain a clear scanning image. Scraping and tapping did not work well enough to get rid of the bigger, loose particles. Therefore, the final step of blasting the samples with compressed air was added to the preparation process. After this, clear scanning images were obtained of the small particles, which were around or below 5 µm in size.

### Buffer check

In order to check if a buffered solution was needed for the dissolution experiment, a small amount of sample (5 µL) was mixed with 50 mL of a non-buffered 0.1 M sodium chloride solution. The pH of the solution was measured before addition of the sample and for half an hour after. The pH changed from the initial value of 4.54 to a value of 9.42 during the first 15 minutes. After this, the rise in pH continued, albeit at a considerably slower rate. As the main aim of the experiment is to see the differences in dissolution between the samples and we want to replicate the resorption conditions of the osteoclast as much as possible, it is important to keep the pH a stable factor. Therefore, this change in pH confirms the importance of using a buffered solution during the dissolution experiment.

### AFM dissolution experiment

The set-up of the fluid cell proved to be difficult using the original silicon wafers, as they were too small for the O-cell to fit onto the wafer surface itself. Instead, the silicon wafer had to be mounted onto a glass plate and onto the metal sample plate so that the O-ring could fit around the silicon wafer and stick to the glass plate. However, as the wafer is about 2-3 mm thick, the tip could not be moved down enough to cause a sufficient amount of compression on the O-ring which therefore didn't adhere to the surfaces enough. This resulted in multiple leaks during set-up of the experiment. The use of a different type of silicon wafer, which was bigger and could be cut to the required size, solved this problem. The wafers were cut with a glass cutter so that it could still fit in the AFM fluid cell, but was also big enough for the O-ring to fit onto. Precipitation of the sample powders onto the newly constructed silicon wafer was done in the same way as before, using a pipette, spraying it with isopropanol and blowing it with compressed after the powder had dried.

Next, the silicon wafer was mounted onto a metal plate and placed on the sample holder, which was covered with plastic to protect the electronic parts of the AFM from any leaking fluids. After checking and/or replacing the tip in the fluid cell, some silicon compound was placed in the groove around the tip to hold the silicon O-ring in place. More silicon compound was put on the outer edge of the O-ring as well. The fluid pump was placed next to the AFM, holding a 20 mL syringe filled with the sodium chloride solution, which was prepared earlier. Then, the fluid cell was secured onto the AFM instrument and the tip brought down to the surface. To prevent any air bubbles to get stuck under the cantilever, the tip was brought up about 5 taps before attaching the laser and making sure it is roughly aligned. Then, the pump was started with a rate of 0.5 ml/hour. Once the tube had filled up and fluid is about to drip out at the end, it was placed in the fluid cell. Continue to check for leaks while the cell is starting to fill up. Put in the outlet tube once it has completely filled with fluid. Continue to check for leaks and turn the pump rate down to 0.1 ml/hour. Finally, the tip can be brought down to the surface, and the laser can be correctly aligned.

### Determination carbonate type and content

The $v_2CO_3/v_3PO_4$ ratio that was used to determine the carbonate content from the FTIR data was calculated in several steps. First, the total area of the $v_2CO_3$ domain was calculated by deconvolution of this domain. A consistent way of deconvolution is important to minimize the variation in which the software finds the best fit to the peaks. After trying it in several different ways, the best method seemed to be as follows: load the normalized FTIR data into Fityk and de-activate the whole area except for the part between 860 and 890 $cm^{-1}$. Then, put in three peaks centred at 866, 872 and 878 and lock the centre variable. These peaks represent the type A, type B and labile substitutions of carbonate respectively. Put the height and width variables at 0.1 and the shape at 1, and leave them unlocked. Next, auto-fit the peaks, unlock the centre variables and auto-fit again. Use the same method for all samples. Compare the results to the literature and make sure it fits the expectations. When the deconvolution is done right, adding the peak surface areas of the smaller peaks results in the total area of the $v_2CO_3$ domain for that sample. The same method was used to determine the area of the $v_3PO_4$ domain, only here one peak was used for deconvolution. Lastly, dividing the total area of the $v_2CO_3$ domain by the $v_3PO_4$ domain gives the ratio.

The results from the $v_2CO_3$ deconvolution are also used to calculate the ratios of the different types of carbonate substitution, as dividing the corresponding peak by the total domain area gives the relative amount of A-, B- or labile substitution type.

# Appendix B. Raw data

## pH measurements

| Sample / Initial pH | CaCl solution | $PO_4$ solution | | Sample / pH | 1 | 2.5 | 5 | 10 | 15 | 30 | 45 | 60 |
|---|---|---|---|---|---|---|---|---|---|---|---|---|
| **CO0** | 8.85 | 9.11 | | **CO0** | 6.00 | 5.25 | 5.17 | 5.15 | 5.11 | 5.09 | 5.08 | 5.08 |
| **CO1** | 8.85 | 10.98 | | **CO1** | 10.13 | 10.11 | 10.08 | 10.07 | 10.05 | 10.02 | 10.01 | 9.99 |
| **CO2** | 8.85 | 10.92 | | **CO2** | 10.48 | 10.48 | 10.48 | 10.48 | 10.48 | 10.43 | 10.41 | 10.40 |
| **CO3** | 8.85 | 10.94 | | **CO3** | 10.66 | 10.66 | 10.65 | 10.64 | 10.62 | 10.60 | 10.62 | 10.60 |
| **CO4** | 8.85 | 10.89 | | **CO4** | 10.68 | 10.69 | 10.70 | 10.71 | 10.70 | 10.69 | 10.66 | 10.64 |

## Spectroscopic analysis

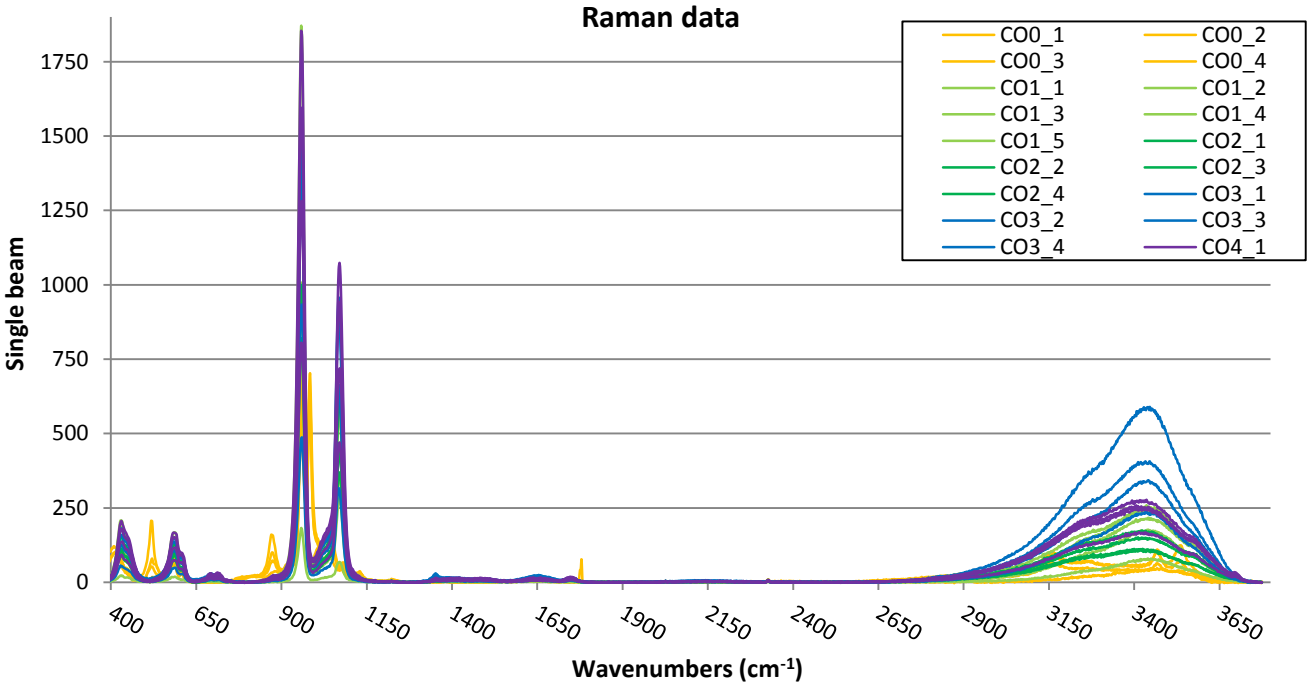


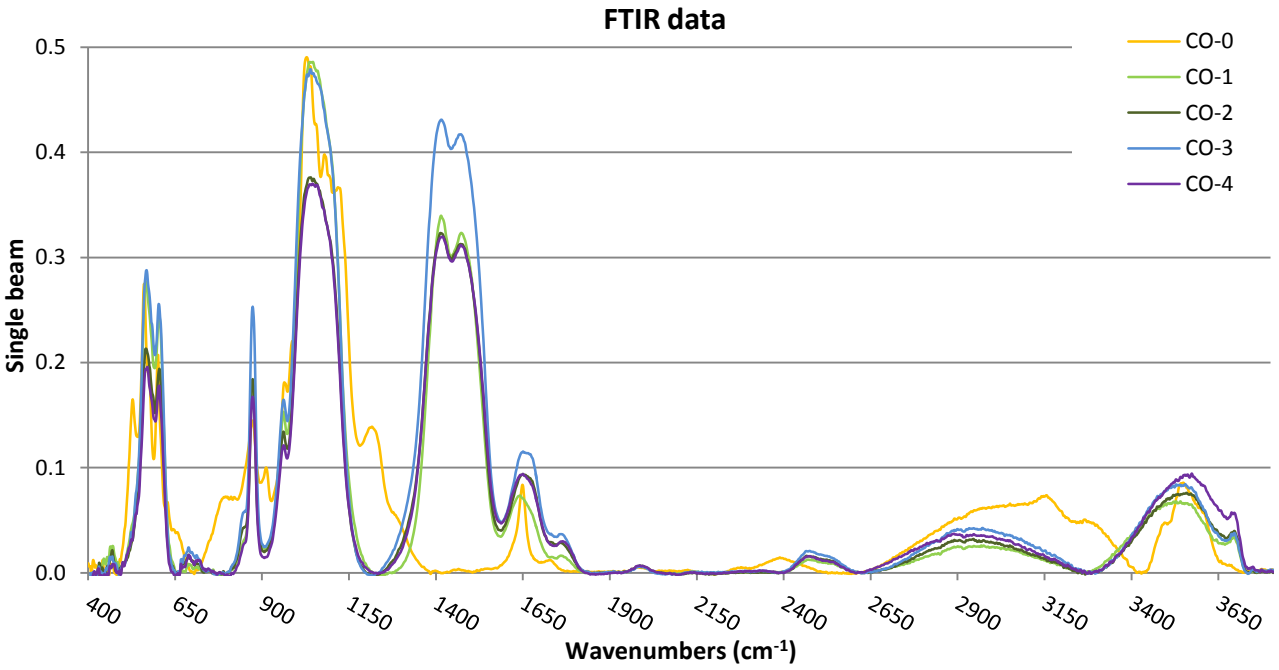

## Phosphate measurements

| Sample | Absorbance | 0 | 5 | 10 | 20 | 30 | 45 | 60 | 75 | 90 | 120 | 150 | 180 |
|---|---|---|---|---|---|---|---|---|---|---|---|---|---|
| **CO0** | **Results 1** | 0.000 | 0.146 | 0.165 | 0.174 | 0.180 | 0.177 | 0.181 | 0.179 | 0.175 | 0.189 | 0.185 | |
| | **Results 2** | 0.000 | 0.159 | 0.175 | 0.180 | 0.185 | 0.185 | 0.185 | 0.186 | 0.187 | 0.187 | 0.188 | 0.187 |
| | **Mean** | 0.000 | 0.153 | 0.170 | 0.177 | 0.183 | 0.181 | 0.183 | 0.183 | 0.181 | 0.188 | 0.187 | |
| **CO1** | **Results 1** | 0.000 | 0.060 | 0.092 | 0.112 | 0.125 | 0.129 | 0.130 | 0.131 | 0.131 | 0.125 | 0.138 | |
| | **Results 2** | 0.000 | 0.065 | 0.101 | 0.126 | 0.151 | 0.158 | 0.158 | 0.160 | 0.165 | 0.165 | 0.164 | 0.163 |
| | **Mean** | 0.000 | 0.063 | 0.097 | 0.119 | 0.138 | 0.144 | 0.144 | 0.146 | 0.148 | 0.145 | 0.151 | |
| **CO2** | **Results 1** | 0.000 | 0.079 | 0.109 | 0.126 | 0.133 | 0.135 | 0.134 | 0.134 | 0.138 | 0.139 | 0.134 | |
| | **Results 2** | 0.000 | 0.063 | 0.100 | 0.122 | 0.143 | 0.154 | 0.154 | 0.156 | 0.157 | 0.158 | 0.159 | 0.155 |
| | **Mean** | 0.000 | 0.071 | 0.105 | 0.124 | 0.138 | 0.145 | 0.144 | 0.145 | 0.148 | 0.149 | 0.147 | |
| **CO3** | **Results 1** | 0.000 | 0.083 | 0.112 | 0.112 | 0.122 | 0.123 | 0.121 | 0.108 | 0.123 | 0.113 | 0.125 | |
| | **Results 2** | 0.000 | 0.097 | 0.135 | 0.139 | 0.143 | 0.153 | 0.153 | 0.153 | 0.155 | 0.152 | 0.152 | 0.150 |
| | **Mean** | 0.000 | 0.090 | 0.124 | 0.126 | 0.133 | 0.138 | 0.137 | 0.131 | 0.139 | 0.133 | 0.139 | |
| **CO4** | **Results 1** | 0.000 | 0.065 | 0.096 | 0.113 | 0.121 | 0.121 | 0.113 | 0.116 | 0.120 | 0.123 | 0.118 | |
| | **Results 2** | 0.000 | 0.065 | 0.106 | 0.124 | 0.142 | 0.149 | 0.150 | 0.152 | 0.152 | 0.152 | 0.151 | 0.148 |
| | **Mean** | 0.000 | 0.065 | 0.101 | 0.119 | 0.132 | 0.135 | 0.132 | 0.134 | 0.136 | 0.138 | 0.135 | |

## Spectroscopic analysis of dissolved particles